

JET-INDUCED SHOCKS IN 3C 171: AN INTERMEDIATE-REDSHIFT ANALOG OF HIGH-REDSHIFT RADIO GALAXIES

N. E. CLARK^{1,2} AND D. J. AXON^{1,3}

Space Telescope Science Institute, 3700 San Martin Drive, Baltimore, MD 21218; nclark@stsci.edu, axon@stsci.edu

C. N. TADHUNTER

Department of Physics, University of Sheffield, Hicks Building, Hounsfield Road, Sheffield S3 7RH, UK; c.tadhunter@sheffield.ac.uk

A. ROBINSON

Department of Physical Sciences, University of Hertfordshire, College Lane, Hatfield, Herts, AL10 9AB, UK; ar@star.herts.ac.uk

AND

P. O'BRIEN

Department of Physics and Astronomy, Leicester University, University Road, Leicester LE1 7RH, UK; pto@star.le.ac.uk

Received 1997 May 2; accepted 1997 September 29

ABSTRACT

We present spectroscopic observations of the extended emission-line region (EELR) aligned with the radio axis of the powerful radio galaxy 3C 171. The results obtained from a detailed analysis of the observational data show that shocks induced by jet-cloud interactions have a dramatic effect on the extended line-emitting gas. The evidence for shocks includes (1) close radio-optical associations; (2) ionization minima coincident with both radio hot spots; (3) high-velocity ($\sim 500 \text{ km s}^{-1}$) line splitting displaced by $\sim 2''$ (10 kpc) (a Hubble constant of $H_0 = 50 \text{ km s}^{-1}$ and a deceleration parameter of q_0 are assumed throughout this paper) behind the hot spots on either side of the nucleus, spatially associated with the two inner radio knots; (4) large line widths in the extended gas (FWHM $\sim 1300 \text{ km s}^{-1}$); and (5) an anticorrelation between line width and ionization state in the extended gas. Given that shocks clearly determine the morphology, kinematics, and physical conditions of the extended line-emitting gas, shock ionization is a possible alternative to AGN photoionization in the EELR. The high [O III] temperatures and low He II/H β ratios in the EELR provide evidence that local ionization by shocks is indeed important.

A pronounced UV continuum excess is also detected in the extended line-emitting regions. From the measured strength of the Balmer lines, it is found that the extended UV continuum is dominated by nebular continuum emission from the warm gas. There is no evidence whatsoever for jet-induced star formation.

The properties of 3C 171—in particular the alignment of the optical line and UV-continuum emission with the radio axis, and the extreme emission-line kinematics in the extended gas—are similar to those observed in high-redshift radio galaxies. This supports the hypothesis that jet-induced shocks determine the distribution, kinematics, physical conditions, and ionization of the EELR in the powerful radio galaxies observed at high redshifts.

Subject headings: galaxies: active — galaxies: individual (3C 171) — galaxies: jets — shock waves

1. INTRODUCTION

It has been proposed that the extended emission-line regions (EELR) around powerful radio galaxies represent ambient gas in the halos of the host galaxies that has been illuminated by a central (anisotropic) continuum source (see, e.g., Fosbury 1989). This hypothesis appears to be consistent with the observed morphologies and emission-line ratios of the majority of *low-redshift* ($z < 0.1$) radio galaxies (Robinson et al. 1987; Binette, Wilson, & Storchi-Bergmann 1996; Simpson & Ward 1996). However, EELR are particularly prevalent in powerful, high-redshift ($z > 0.5$) radio galaxies (McCarthy 1988), and the properties of these EELR are markedly different from those observed

at low redshifts. First, the EELR are often accurately aligned with the axes of the extended radio emission (McCarthy et al. 1987). Such precise alignments, with the EELR apparently being closely confined to the radio axes, are contrary to what would be expected for illumination of an isotropic gaseous halo by the broad radiation cones predicted by unified schemes relating radio galaxies to quasars (Barthel 1989). Second, extreme emission-line kinematics are observed along the radio axes in the majority of high-redshift radio galaxies (van Ojik 1995; McCarthy, Baum, & Spinrad 1996). This is in contrast to the situation in nearby sources, in which the gas kinematics generally appear to be consistent with gravitational motions (Tadhunter, Fosbury, & Quinn 1989; Baum, Heckman, & van Breugel 1992).

An alternative to AGN illumination invokes the shocks produced by violent interactions between the advancing radio jet and the ambient ISM (de Young 1981, 1986; van Breugel et al. 1985, 1986; Meisenheimer & Hippelein 1992; Sutherland, Bicknell, & Dopita 1993; Dopita & Sutherland 1995). The passage of the radio jet through the ISM drives strong shock waves into warm clouds of gas embedded in

¹ Affiliated with Astrophysics Division, Space Science Department of ESA, ESTEC, 2200 AG Noordwijk, The Netherlands.

² Some of the work for this paper was carried while the author was a research associate at Department of Physics, University of Sheffield, Hicks Building, Hounsfield Road, Sheffield S3 7RH, UK.

³ On leave from The Nuffield Radio Astronomy Laboratory, University of Manchester, Jodrell Bank, Macclesfield, Cheshire SK11 9DL, UK.

TABLE 1
GLOBAL PROPERTIES OF 3C 171

| Parameter | Value |
|---|----------------------|
| Redshift | 0.2381 |
| Linear–angular scale ratio (kpc arcsec ^{−1}) | 5.05 |
| Absolute visual magnitude, M_v | −20.9 |
| E_{B-V} (field) | 0.06 |
| Flux density (1400 MHz) (Jy) | 3.8 |
| Monochromatic power (1415 MHz) (ergs s ^{−1} Hz ^{−1}) | 9.3×10^{33} |
| Total radio luminosity (10^7 – 10^{11} Hz) (ergs s ^{−1}) | 10^{44} |
| Radio spectral index, α | −0.94 |

the hot halo of the galaxy. The shocks rapidly heat, compress, and accelerate the gas clouds and the enveloping halo gas. The shocked gas is likely to be a strong source of line emission because the postshock clouds cool by emitting line radiation and the clouds are also subjected to an intense local ionizing radiation field from the hot ($>10^6$ K) shocked gas.

The extreme properties of the EELR in high-redshift radio galaxies are consistent with the jet-cloud interaction model outlined above. However, although shocks apparently play a role in high-redshift radio galaxies, the detailed effects of jet-cloud interactions in these sources—and in particular the balance between AGN photoionization and shock ionization—are difficult to determine. High-redshift radio galaxies are difficult to study, because (1) they have small angular sizes and the emission-line fluxes are low (problems that have recently been alleviated somewhat by *Hubble Space Telescope* [*HST*] and large ground-based telescopes, respectively); and (2) the rest-frame optical spectra (including important diagnostic emission lines) are redshifted to the infrared.

These problems disappear when we move to lower redshifts. In an attempt to learn more about the physical processes occurring in these sources, we have made a detailed study of a small sample of relatively nearby radio galaxies that share many of the properties of high-redshift radio galaxies. The data allow us to study the physics of jet-cloud interactions and hence to determine the effects of these interactions upon the morphology, kinematics, physical conditions, and ionization of the extended line-emitting gas.

In a previous paper, results were presented for the powerful radio galaxy PKS 2250–41 (Clark et al. 1997). The data presented in this paper comprise new, high-quality optical long-slit spectra of 3C 171, a source that appears to be an intermediate-redshift prototype of the high-redshift radio galaxies. These data are complemented by optical and radio imaging data, which allows us to make an in-depth study of the jet-cloud interactions in 3C 171. In the following section, previous observations of 3C 171 are summarized. In § 3 we give details of the new observations and data reduction, and the results are presented in § 4. Finally, in § 5

we discuss these results, and the properties of 3C 171 are compared with those of other radio galaxies—particularly those at high redshifts.

2. PREVIOUS OBSERVATIONS OF 3C 171

The basic properties of 3C 171, a powerful FR II radio galaxy with a redshift $z = 0.2381$, are listed in Table 1 (from data presented by Kuhr et al. 1979, by Véron-Cetty & Véron 1993, and in this paper). Evidence of a jet-cloud interaction was revealed by the first detailed study of this sources by Heckman, van Breugel, & Miley (1984; hereafter H84). Optical images (H84; Baum et al. 1988) showed line emission extending along the radio axis, with a spatial extent similar to that of the radio emission. The radio emission from 3C 171 also has an unusual morphology: a plume of radio emission is seen to extend, perpendicular to the radio axis, some 20" north of the western hot spot, with similar plumes north and south of the eastern hot spot (H84; Blundell 1994, 1996). The total extent of the radio emission along the radio axis of 3C 171 is only 11".4 (58 kpc), unusually compact for a powerful FR II source. In addition to the radio and optical morphologies, evidence for jet-cloud interactions was provided by the optical long-slit spectra, which revealed complex emission-line kinematics (large line widths and sudden jumps in velocity) in the extended gas. However, because of the poor quality (low signal-to-noise ratio [S/N] and low resolution) of the previous optical data, it was not possible to study the nature of the interactions or the effects on the line-emitting gas in any detail.

3. OBSERVATIONS, DATA REDUCTION, AND ANALYSIS

Long-slit spectra of 3C 171 were obtained using the ISIS dual-beam spectrograph and CCD detectors on the 4.2 m William Herschel Telescope on La Palma. Details of these observations, made in three separate runs, are summarized in Table 2. The spectrograph slit was aligned parallel to the axis of the extended radio emission (PA 102°); the projected slit position is shown superimposed on a broadband *HST* image of 3C 171 in Figure 2 (*top*).

TABLE 2
DETAILS OF THE OPTICAL SPECTROSCOPIC OBSERVING RUNS

| Dates | Time (s) | CCD | Grating | Seeing (arcsec) | Slit (arcsec) | λ Range (Å) | Pixel Scale (arcsec Å ^{−1}) |
|----------------------|----------|------|---------|-----------------|---------------|---------------------|---------------------------------------|
| 1990 Jan 20–24 | 9000 | EEV2 | 158R | 1.3 | 1.3 | 5600–8694 | 0.335/2.70 |
| 1992 Jun 23–26 | 7200 | Tek1 | 158B | 1.3 | 1.3 | 3930–6900 | 0.358/2.88 |
| 1993 Jan 25–28 | 7200 | EEV3 | 600R | 1.3 | 1.3 | 5360–6280 | 0.335/0.74 |
| | 7200 | EEV3 | 600R | 1.3 | 1.3 | 7630–8550 | 0.335/0.74 |

The long-slit spectra were reduced in the standard manner using the Starlink FIGARO data reduction package on Sun workstations at the University of Sheffield. The procedures involved were bias subtraction, flat-fielding, cosmic-ray removal (manually using the CLEAN routine), wavelength calibration (using ARC2D), extinction correction, flux calibration, vignetting correction, and sky subtraction. The source was observed close to the zenith to minimize the effects of differential refraction. The final long-slit spectrum for each combination of dispersion and spectral range results from co-adding a series of individual observations with the *total* exposure times listed in Table 2.

The low-dispersion long-slit spectra were analyzed by fitting single Gaussians to the line profiles using the Starlink LONGSLIT spectral analysis package, which yielded maps of the gross kinematic and physical condition variations as a function of location. The high-dispersion spectra were analyzed using the DIPSO package, which allows greater flexibility when constraining multicomponent fits. Spectral slices were extracted from the long-slit spectra, and multiple Gaussians were then fitted to the emission-line profiles in order to analyze the complex kinematic structure of 3C 171. The general philosophy of the fitting procedure was first to obtain a good fit, using as few components as possible, to strong, unblended lines such as [O III] $\lambda\lambda 4959$, 5007 and H β . It was then assumed that the same kinematic components were present in all of the line profiles, with only the relative strength of the different components varying from one line to another. The blended and weaker lines were then fitted—first unconstrained if the S/N permitted, and then with line widths and velocity shifts constrained by the results obtained from the stronger lines. The fitted profiles obtained in this way were in agreement with the data, consistent with the assumption of identical components. The resulting intensity and velocity information was then analyzed.

The measured line widths were all corrected in quadrature for instrumental broadening. The instrumental widths—derived from the night-sky lines, and verified using arc lines—are 2.23 Å for the high-dispersion blue data, 2.19 Å for the high-dispersion red data, 8.55 Å for the low-dispersion blue data, and 8.90 Å for the low-dispersion red data. No systematic variations are seen in the widths of sky lines in either the spatial or the spectral directions.

The errors in the measured line fluxes, line widths, and velocity shifts quoted in this paper are the 1σ errors computed by the fitting routines (due to noise in the data and the uncertainties in the Gaussian fitting procedure). To illustrate the accuracy of the fitting process for strong lines, the measured variation in the [O III](5007)/[O III](4959) emission-line ratio along the radio axis is plotted for the low-dispersion red and blue data sets in Figure 1. It can be seen that the measured values are consistent—to within the errors returned by the fitting software—with the theoretical value (set by atomic physics at 2.88), and the scatter about the theoretical value is consistent with the error bars.⁴ The two [O III] lines are closely spaced in wavelength, however, and the uncertainties due to inaccuracies in the flux calibration may be larger for lines more widely separated in wavelength. This was of particular concern for the low-dispersion red data—because the order-sorting filter was

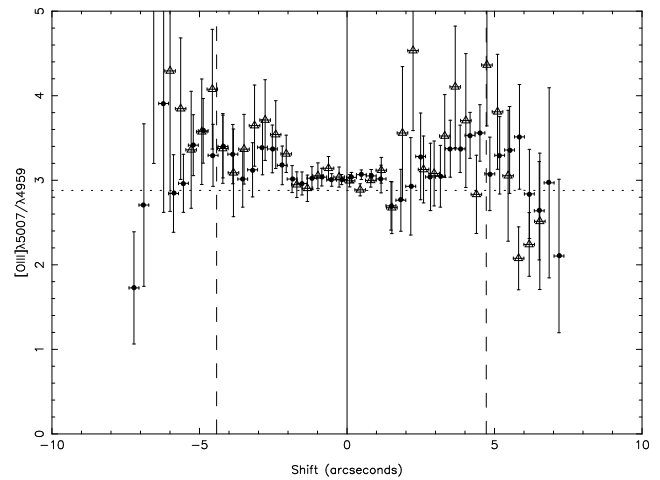


FIG. 1.—Graph showing the [O III] $\lambda 5007$ /[O III] $\lambda 4959$ ratios measured along the radio axis for the long-slit spectra of 3C 171, compared with the theoretical value of 2.88, for the low-dispersion blue data (*open triangles*) and red data (*filled circles*). In this and all subsequent line plots (unless indicated otherwise), the x-axis denotes the displacement from the optical continuum centroid—west is to the right—and the positions of the radio hot spots are indicated by dashed vertical lines.

not in the optical path during the observations—but the line fluxes measured from this data set are in good agreement with those measured from the other long-slit spectra. From a comparison of the calibration frames, we estimate that uncertainties of up to $\sim 10\%$ are possible in the relative flux calibration within each data set.

In order to ascertain the effects of structure in the underlying stellar continuum emission on the observed emission-line spectra, an elliptical galaxy template spectrum was subtracted from the spectra of 3C 171, scaled to the 4000 Å break for the blue spectrum and to the strength of the stellar absorption features for the red spectrum. However, the emission lines have large equivalent widths—particularly in the extended gas—and in general this subtraction had only a minor effect on the measured line fluxes (for example, the continuum subtraction reduces the H β flux in the nucleus by less than 2%).

4. RESULTS

4.1. HST Imaging of 3C 171

A broadband image of 3C 171 has been obtained with the WFPC2 on board the *HST* as part of a snapshot survey of 3C radio galaxies (de Kopf et al. 1996). This image, with a spatial resolution of approximately $0''.1$, allows a more detailed study of the extended emission-line and continuum structures than has been previously possible. The broadband filter used for the *HST* observation (F702W) includes both continuum emission and line emission (mainly from [O III] $\lambda 5007$, plus H β , H α , and [N II] $\lambda\lambda 6548$, 6583). A gray-scale representation of the co-added image is plotted in Figure 2 (*top*) (Plate 21).

Although the individual features in the *HST* image are not oriented exactly parallel to the radio axis, the degree of collimation along the radio axis of 3C 171 is striking—the total extent of the brightest features along the axis is approximately $11''$, whereas the perpendicular extent is less than $2''$. On large scales, filaments and knots can be seen extending along the radio axis $2''$ – $5''.5$ east and west of the nucleus, and distinct curved filaments are also seen closer to

⁴ There is a slight bias toward higher values away from the nucleus; this is apparently due to low S/N in the wings of the [O III] $\lambda 4959$ line.

the nucleus, again extending approximately east-west. A comparison of this high spatial resolution broadband image with the (lower resolution) ground-based data presented below indicates that the extended filaments are due mainly to line emission, while the central core emission consists of both line and continuum emission. The aligned linear features of 3C 171 bear a striking resemblance to similar features visible in *HST* images of the archetypal powerful high-redshift ($z = 1.135$) radio galaxy 3C 368 (Longair, Best, & Rottgering 1995), as is discussed further in § 5.4.

It is important to point out that not all of the extended emission along the radio axis of 3C 171 is concentrated in the bright knots/filaments seen in the *HST* image. For instance, only $\sim 46\%$ of the flux emitted more than $3''.5$ east of the nucleus is contained within the bright filament centered at a radius of $4''.4$. Almost half of the flux at a distance of more than $2''.2$ from the nucleus ($r > 11$ kpc) comes from diffuse material, although we estimate that approximately 50% of this diffuse component may be due to stellar continuum emission from the halo of the host galaxy.

Two unresolved point sources are observed in the *HST* image, located $4''.0$ east of the nucleus along PA 83° and $3''.0$ southwest of the nucleus along PA 221° . Since they are unresolved, they are most probably foreground stars. The star to the southwest lies $2''.6$ from the radio axis and therefore will not seriously contaminate the long-slit spectra. The star to the east, however, lies only $1''.3$ north of the slit position and is detected in our long-slit spectra (see § 4.6).

A contour plot of the 8 GHz radio map of 3C 171 is shown superimposed on a gray-scale representation of the *HST* image in Figure 2 (*bottom*). In registering the radio and optical images, we have assumed the radio core to be coincident with the centroid of the brightest nuclear concentration in the optical images. There is clearly a close spatial association between the radio emission and the optical line emission: the eastern radio hot spot is located only $\sim 0''.4$ to the north of the associated emission-line filament, and the western hot spot lies just beyond the end of the long western emission-line filament.

Radio studies of 3C 171 have shown that the depolarization ratio is low along the length of the radio axis (H84; Blundell 1994), with a steady decrease in the amount of depolarization with distance from the radio axis. It is evident from a comparison of the depolarization structure with the spatial distribution of the line-emitting gas seen in the *HST* image that the regions of bright line emission are closely correlated with regions of large depolarization measure. This suggests that the radio emission is depolarized by the clouds of warm emission-line gas, owing to differential Faraday rotation either by an external screen or by clouds internal to the radio plasma.

4.2. Long-Slit Spectroscopy: The Optical Emission-Line Structure

Gray-scale representations of our new long-slit spectra of 3C 171 are presented in Figures 3–4 (Plates 22–23). The spatial profiles of the line emission derived from these long-slit spectra are presented in Figure 5. Line emission is seen extending approximately $14''$ (71 kpc) along the radio axis, with a central nuclear peak and separate peaks to the east and the west of the nuclear continuum centroid. The spatial profiles were derived in two different ways: first, by extracting one-dimensional spectra for each spatial pixel and fitting single Gaussians to the emission line profiles, and

second, by extracting spatial slices through the long-slit spectra. The spatial slices were derived by extracting a 60 \AA wide slice, perpendicular to the dispersion direction, centered on the appropriate emission line, and then subtracting a slice of equal width from an adjacent line-free region of the spectrum to correct for continuum contamination. There are no significant differences between the profiles derived from the different data sets for a given emission line. There are, however, differences between the profiles obtained by extracting spatial slices through the long-slit spectra and those derived by fitting single Gaussians to the emission line profiles. This is because the single Gaussian fits exclude the broad wings of line emission observed in the EELR (see § 4.3).

The central peak in the line emission is coincident, within the errors, with the nuclear continuum centroid. In addition to this central peak, the spatial emission-line profiles show pronounced peaks $\sim 3''$ west and $\sim 4''$ east of the nucleus. It is notable that the off-nuclear (EELR) peaks are higher relative to the central peak in the low-ionization ([O II], [O I], [N II] and [S II]) and Balmer lines than in [O III], which indicates that the average ionization state is lower in the EELR than in the nucleus (see § 4.4). More intricate substructure can also be seen in the EELR emission: in particular, an inner subpeak is evident in the line profiles approximately $3''$ to the east of the nucleus. The projected positions of the radio hot spots are also indicated in Figure 5, which shows that the western EELR peak occurs closer to the nucleus than the radio hot spot, whereas the positions of the eastern EELR peak and radio hot spot are closely associated.

The variation of the flux along the radio axis derived from the broadband *HST* image of 3C 171 (obtained by extracting a slice along the radio axis from the *HST* image, with a width equal to the slit width of $1''.3$) is plotted for comparison in Figure 5. The *HST* data agree well with the variations in line flux measured from the lower resolution long-slit spectra (bearing in mind the much higher resolution of the *HST* data and the continuum contamination present in the broadband image).

4.3. Long-Slit Spectroscopy: The Emission-Line Kinematics

The kinematics of the emission-line gas in 3C 171 are discussed in detail in this section. The spectra were all shifted to the 3C 171 rest frame before kinematical analysis, and the velocities and line widths presented are all rest-frame values. The redshift derived for 3C 171 from single-Gaussian fits to the high-dispersion line profiles within a $1''.5$ radius of the nucleus is $z = 0.2381 \pm 0.0001$.

4.3.1. Low-Dispersion Spectra

Kinematic information was extracted from the blue and red low-dispersion spectra by fitting single Gaussians to the emission-line profiles. The resulting variations in the velocity centroids along the radio axis of 3C 171 are plotted in Figure 6. Two points are immediately apparent from this diagram. First, the velocity field appears complex and chaotic—in particular, there is a sudden large jump in velocity $\sim 3''$ west of the nucleus. Second, the most striking aspect of Figure 6 is the *clear contrast in the velocity centroids of the high-ionization [O III] $\lambda 5007$ line emission with respect to the low-ionization [O II] $\lambda 3727$ and [O I] $\lambda 6300$ emission in the extended gas.* The [O I] and [O II] line

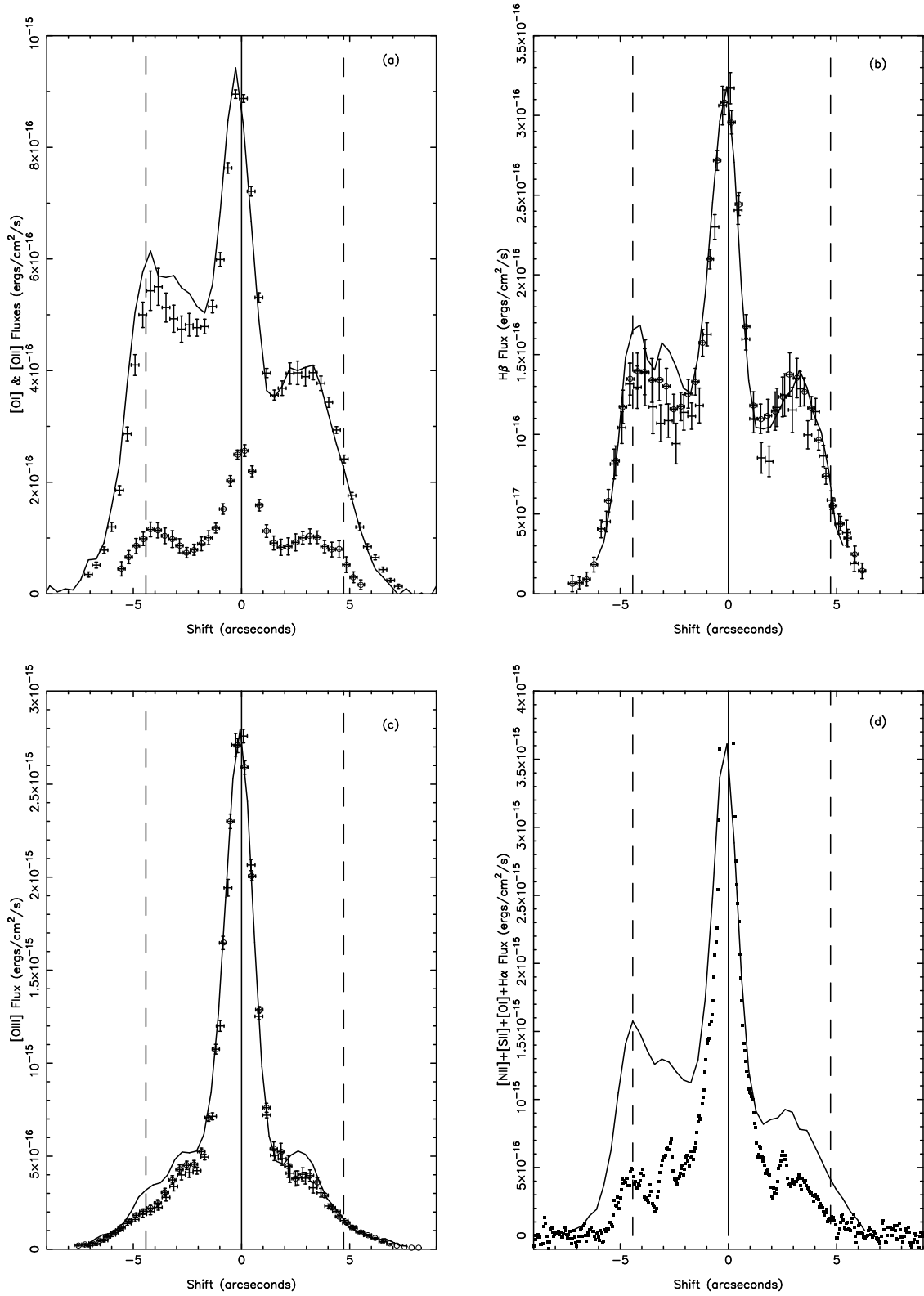


FIG. 5.—Variation in the strength of the strong emission lines along the radio axis of 3C 171. (a) The $[\text{O II}]$ $\lambda 3727$ spatial profile from the blue low-dispersion spectrum, derived (1) by fitting single Gaussians to the spectral profiles along the radio axis (crosses) and (2) by extracting a spatial slice through the long-slit spectrum (solid line). The $[\text{O I}]$ profile from the red low-dispersion data, derived by fitting single Gaussians, is shown for comparison (circles). (b) The $\text{H}\beta$ spatial profile, obtained by (1) fitting single Gaussians to the spectral profiles along the radio axis for the blue (crosses) and red (circles) low-dispersion data and (2) by extracting a slice through the blue high-dispersion data (solid line). (c) The $[\text{O III}]$ $\lambda 5007$ spatial profile—symbols as in (b). (d) The variation in the sum of the flux from the $[\text{O I}]$ $\lambda 6300$, $[\text{N II}]$ $\lambda\lambda 6548, 6583$, $[\text{S II}]$ $\lambda\lambda 6717, 6731$, and $\text{H}\alpha$ lines from the red high-dispersion spectrum (solid line), compared with the emission along the radio axis from the broadband *HST* image (squares).

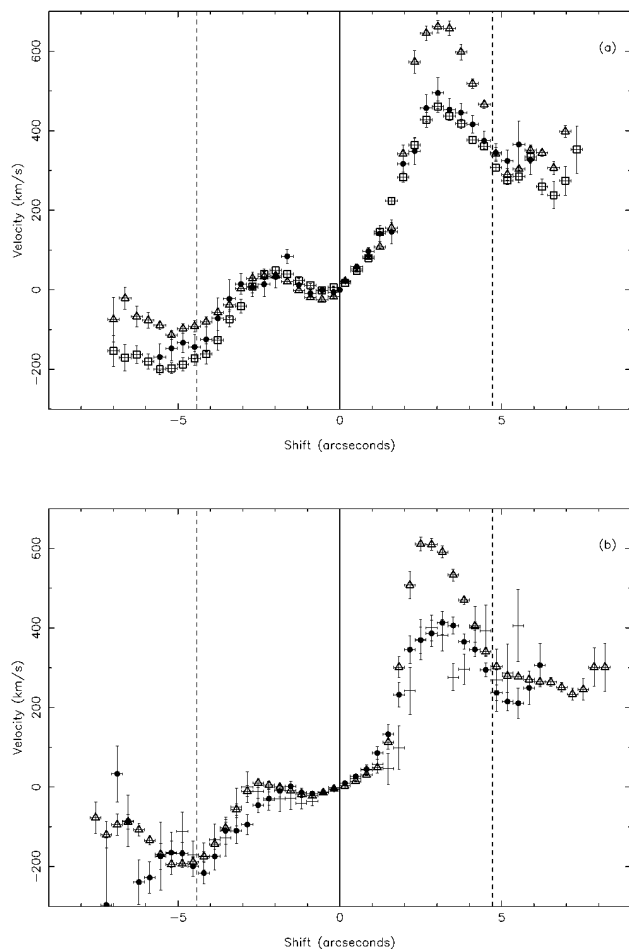


FIG. 6.—Variation in the rest-frame velocity centroids along the radio axis of 3C 171, from (a) the blue low-dispersion spectrum, for [O II] $\lambda 3727$ (open squares), [O III] $\lambda 5007$ (open triangles), and H β (filled circles); and (b) the red low-dispersion spectrum, for the lines [O I] $\lambda 6300$ (crosses), [O III] $\lambda 5007$ (open triangles), and H β (filled circles).

centroids are blueshifted by $\sim -200 \text{ km s}^{-1}$ with respect to the central nuclear velocity at the eastern extreme of the EELR, rise gradually toward the nucleus, and then increase steeply to the west to a peak redshift of $\sim 400 \text{ km s}^{-1}$. The [O III] velocity varies in a qualitatively similar manner, but the velocity rises much more steeply to the west, reaching a peak velocity of $\sim 700 \text{ km s}^{-1}$, whereas the peak blueshift to the east is only $\sim 100 \text{ km s}^{-1}$. The observed H β velocity variation appears to be intermediate between that of [O II] and [O III]. For each line, the results obtained from the different data sets are in good agreement; the [O III] velocities also agree with the earlier data of H84.

Figure 7 shows how the line widths of [O II] $\lambda 3727$, [O I] $\lambda 6300$, [O III] $\lambda 5007$, and H β vary along the radio axis. As for the velocity centroids, it is apparent that the line widths of the [O I] and [O II] lines are strikingly different from those of [O III]: *the low-ionization lines are systematically broader than the high-ionization lines throughout the EELR*. The [O III] line width rises to 700 km s^{-1} (FWHM) just east of the nucleus, with a slightly greater rise to the west—this is in general agreement with the less sensitive data of H84. In contrast, the low-ionization [O I] and [O II] line profiles are notably broader in both the eastern EELR (FWHM $\sim 1300 \text{ km s}^{-1}$) and the western EELR (FWHM $\sim 1000 \text{ km s}^{-1}$).

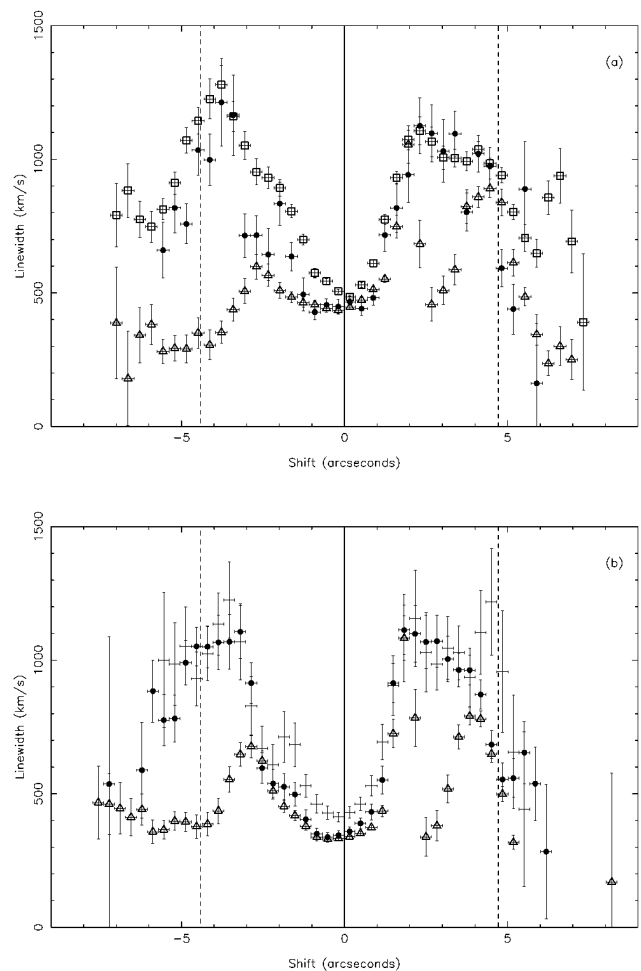


FIG. 7.—Variation in the rest-frame line widths (FWHM) along the radio axis of 3C 171, from the low-dispersion (a) blue and (b) red long-slit spectra. For details, see legend to Fig. 6.

s^{-1}).⁵ The H β line profile in the EELR appears to have a width intermediate between those of the low- and high-ionization lines.

The kinematic behavior of the line-emitting gas in 3C 171 appears complex when studied using a simple one-component velocity fit, with no clear pattern or structure. However, there are signs of line splitting even in our low-dispersion spectra (Fig. 3), and inspection of the high-dispersion long-slit spectra (Fig. 4) reveals a rich and complex kinematic structure, with line emission from a number of distinct kinematical components. The multi-component emission-line system of 3C 171 is discussed in detail in the following section.

4.3.2. High-Dispersion Spectra

The high-dispersion long-slit spectra of 3C 171 improve upon the velocity resolution of the low-dispersion data discussed in the previous section by approximately a factor of 4, and this allows us to make a detailed study of the multi-component emission line kinematics. Some general proper-

⁵ Although [O II] $\lambda 3727$ is actually a blend of two lines, they are separated by only 2.8 \AA or $\sim 200 \text{ km s}^{-1}$. This does not alter the result that the kinematic [O II] line width is similar to that of [O I], and is substantially greater than that of [O III] in the extended gas.

TABLE 3
PROPERTIES OF THE VARIOUS KINEMATIC COMPONENTS IN THE EASTERN AND WESTERN EELR

| Component (1) | Location (2) | Velocity (3) | Line Width (4) | [O III]/H β (5) | [O III] Flux (6) |
|-------------------|---------------------|-----------------|-------------------|--------------------------|---------------------|
| Eastern EELR | | | | | |
| Broad | 2.0–5.0 | –160 | 1400 | 1–3 | 134 |
| Central | 0.0–7.0 | –80 | 210 | 4–7 | 113 |
| Redshifted | 2.0–3.7 | +630 | 200 | ~ 3 | 4 |
| Blueshifted | 2.0–3.7 | –560 | 200 | ~ 9 | 9 |
| Western EELR | | | | | |
| Broad | 1.5–4.0 | +340 | 1200 | 2–3 | 140 |
| Central | 0.0–2.5 and 3.5–7.0 | +100 | 400 | 3–8 | 138 |
| Redshifted | 1.0–4.4 | +680 | 300 | 6–8 | 86 |
| Blueshifted | 2–4 | –470 | 300 | ~ 5 | 3 |

ties of the different kinematic components observed in the extended gas are given in Table 3: Column (1) identifies the component, column (2) gives the observed position (arcseconds from the nucleus), column (3) gives the average velocity centroids (in km s^{-1} relative to the mean nuclear velocity), column (4) gives the estimated line widths (FWHM, km s^{-1}), column (5) gives typical [O III](5007)/H β line ratios, and column (6) gives the total [O III] $\lambda 5007$ flux ($\times 10^{17} \text{ ergs s}^{-1} \text{ cm}^{-1}$) for the given extraction apertures.

The various line-emitting components that are evident in the spectra are as follows:

1. *Central component.*—This component is observed across the full extent of the EELR, from $\sim 7''$ east to $\sim 8''$ west of the nucleus, except for a gap of approximately $2''$ to the west of the nuclear region. The spectral width of this component is approximately 250 km s^{-1} (FWHM) to the east and $\sim 300 \text{ km s}^{-1}$ (FWHM) to the west of the nucleus. The redshift increases smoothly from east to west, with a total velocity amplitude across the nebulosity of $\Delta v \sim 400 \text{ km s}^{-1}$. In the nuclear region, this central component dominates and apparently splits into at least three blended components in the inner arcsecond (a central component and two components symmetrically redshifted and blueshifted from this component by $190 \pm 5 \text{ km s}^{-1}$). From the central nuclear region to approximately $4''$ east of the nucleus, the central component has a pronounced red wing. When an additional Gaussian component is introduced to model this red wing, it is found to be redshifted in the eastern EELR by $\Delta v \sim 220 \text{ km s}^{-1}$ relative to the central nuclear component, with a line width of 390 km s^{-1} .

2. *Broad component.*—This component also extends throughout the EELR, from approximately $6''$ east to $7''$ west of the nucleus, and is relatively strong in the Balmer and low-ionization lines. The width of this component is $\sim 1400 \text{ km s}^{-1}$ (FWHM) in the eastern EELR and $\sim 1200 \text{ km s}^{-1}$ (FWHM) to the west. The velocity centroid varies smoothly along the radio axis and shows a pattern similar to the velocity centroid of the central component.

3. *Split components.*—Redshifted and blueshifted components are observed in both the eastern and western EELR, most clearly in the [O III] line profile. The western redshifted component is the brightest, and is seen even in the low-dispersion spectra (Fig. 3). It extends $1''$ – $4.4''$ west of the nucleus, with a line width of 300 km s^{-1} (FWHM) and a velocity shift of $+680 \text{ km s}^{-1}$ relative to the central nuclear velocity. This component is responsible for the sharp increase in redshift west of the nucleus derived from single-

Gaussian fits to the low dispersion data (Fig. 6; also H84, Fig. 6). The blueshifted component to the west is weak, and consequently the kinematic properties are ill constrained, but it is shifted by approximately -470 km s^{-1} relative to the nuclear velocity, with a width similar to that measured for the brighter redshifted component. In the eastern EELR, a blueshifted component and a fainter redshifted counterpart are also observed, extending from $2.0''$ to $3.7''$ east of the nucleus. The observed line widths are approximately 220 km s^{-1} (FWHM), and the velocity centroids are shifted by $\sim +630 \text{ km s}^{-1}$ and $\sim -560 \text{ km s}^{-1}$, respectively, from the central nuclear velocity.

Examples of the observed H β and [O III] line profiles in the eastern and western EELR, and of the corresponding multiple Gaussian fits, are given in Figure 8. It is clearly important to ensure that all of the components are real (and are not, for instance, relics of the fitting procedure). The central component and the red and blueshifted components can be seen clearly on both the two-dimensional long-slit spectra and the extracted one-dimensional spectra, on either side of the nucleus. The broad component is also clearly visible, as broad wings in the H β profile and in the low-ionization lines of the red high-dispersion spectrum. Even in the low-dispersion spectra, the redshifted western component and the broad component can be fitted, yielding consistent results; as discussed below, it is the existence of this broad low-ionization component that causes the anticorrelation between line width and ionization state seen in the low-dispersion data. The individual components are also visible in the gray-scale ionization map plotted in Figure 15. It is, however, difficult to show unambiguously that these components all have symmetrical Gaussian profiles—while the fits to the data are good, more complex profiles cannot be ruled out.

The best fits were obtained for the [O III] $\lambda\lambda 4959, 5007$ and H β profiles, which could generally be fitted unconstrained. All of the components observed in [O III] and H β emission can also be fitted in the line profiles of [O I] $\lambda 6300$, [N II] $\lambda 6583$, H α , and [S II] $\lambda\lambda 6717, 6731$, and the observed velocity shifts and line widths are consistent with the values derived from the [O III] profile. *The contrasts in the line widths and velocity shifts which are observed in the low-dispersion spectra (Figs. 6–7) can be accounted for by differences in the relative strengths of the separate kinematic components resolved in the high dispersion spectra.*

The variations in the velocity centroids for the different kinematical components observed along the radio axis are

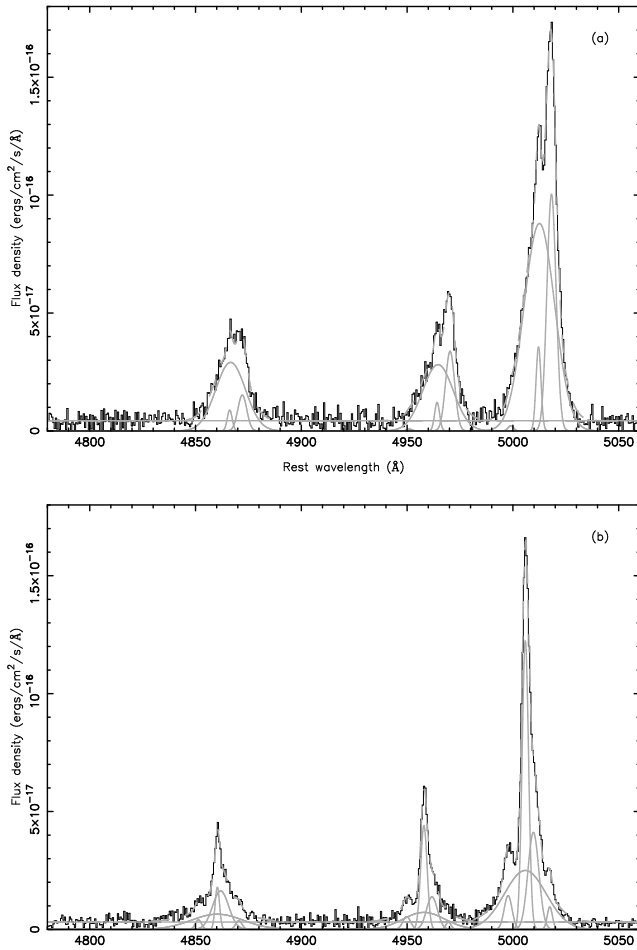


FIG. 8.— $H\beta$, $[O\ III]\ \lambda 4959$, and $[O\ III]\ \lambda 5007$ emission-line profiles (solid black line) from the blue high-dispersion spectrum: (a) eastern EELR ($2''.0 \times 1''.3$ aperture centered $3''.0$ from the nucleus); (b) western EELR ($5''.0 \times 1''.3$ aperture centered $4''.1$ from the nucleus). The solid gray lines represent the multicomponent Gaussian fits to the line profiles (central component, broad component, redshifted and blueshifted components, red wing, and continuum), and the total fit is represented by the dashed gray line. See text for details.

shown in Figure 9a. It is apparent from this figure that the velocity field is actually much more ordered than it appears from the low-dispersion data. In particular, the split components have similar velocities on both sides of the nucleus, and the broad component has a radial velocity distribution that is similar to that of the narrower central component. This symmetry suggests that the systems responsible for the different line-emitting components may have the same origin. The line widths of the various components along the radio axis are plotted in Figure 9b. The line width of the low-ionization broad component does not vary significantly, with $FWHM \sim 1200\text{--}1400\text{ km s}^{-1}$. It also appears that the line widths of the relatively narrow central and the shifted components are generally similar throughout the EELR, $FWHM \sim 200\text{--}400\text{ km s}^{-1}$. The ionization states and the variation in the surface brightness of the different components are discussed in the following section.

4.4. Long-Slit Spectroscopy: The Emission-Line Spectra

Integrated blue and red low-dispersion spectra of the nuclear region and the eastern and western EELR are plotted in Figures 10–11. The integrated fluxes of all of the observed lines in the nucleus and the eastern and western

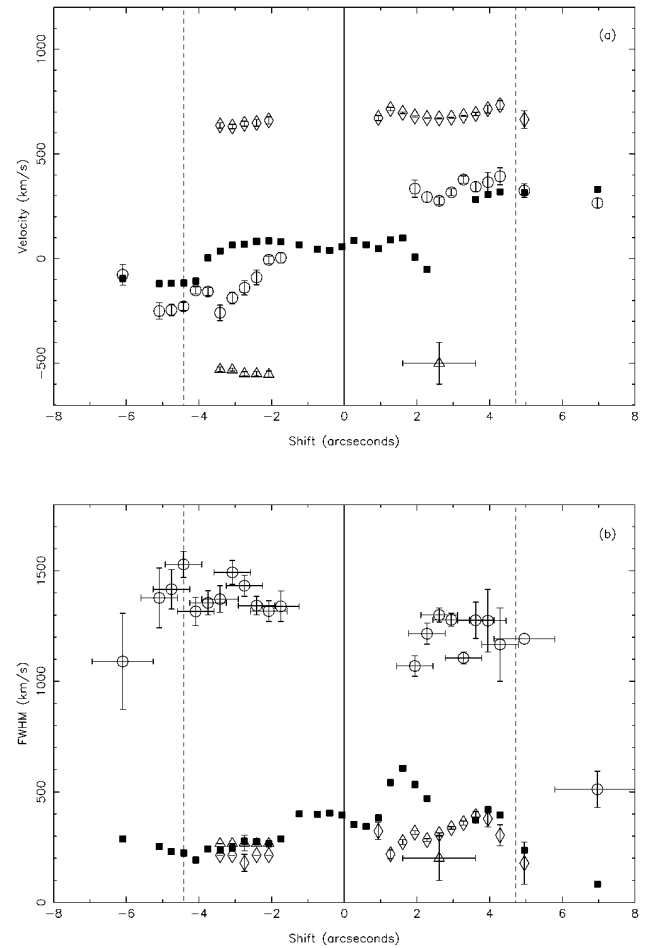


FIG. 9.—Variation in the (a) velocity centroids and (b) line widths (FWHM) along the radio axis for the different kinematic components seen in the $[O\ III]\ \lambda 5007$ emission line, from the blue high-dispersion spectrum. The different components are as follows: broad central component (circles), narrow high-ionization component (filled squares), redshifted component (diamonds), and blueshifted component (triangles). The extraction apertures are plotted for the broad low-ionization component and the western blueshifted component in (b).

EELR are given in Tables 4–5. The fluxes are listed relative to the observed-frame $H\beta$ flux for each aperture, which is given in the bottom row of the table; the nuclear extraction aperture is $3''.2 \times 1''.3$, the extraction aperture for both the eastern and western EELR is $3''.9 \times 1''.3$, centered, respectively, $3''.9$ east and west of the nuclear continuum centroid. The complexity of the line profiles meant that it was not possible to deblend the $H\alpha + [N\ II]\ \lambda\lambda 6548, 6583$ and $[S\ II]\ \lambda\lambda 6717, 6731$ emission-line complexes in the EELR; for this reason, we give only the sum of the emission from these blends. Since both the $H\ I$ maps of Burstein & Heiles (1982) and the $100\ \mu\text{m}$ *IRAS* maps of Rowan-Robinson et al. (1991) indicate low Galactic reddening in the direction of 3C 171 ($E_{B-V} \sim 0.06$) and the observed $H\alpha/H\beta$ and $H\gamma/H\beta$ line ratios are close to the theoretical Case B values along the length of the slit (with the exception of a slight increase in the $H\alpha/H\beta$ ratio coincident with the nucleus which may indicate the presence of a dust lane), no correction for reddening was applied to the data. The line fluxes have, however, been corrected for the underlying stellar continuum, by subtracting a template elliptical galaxy spectrum (1 Gyr burst, 15 Gyr model: Bruzual & Charlot 1993). This

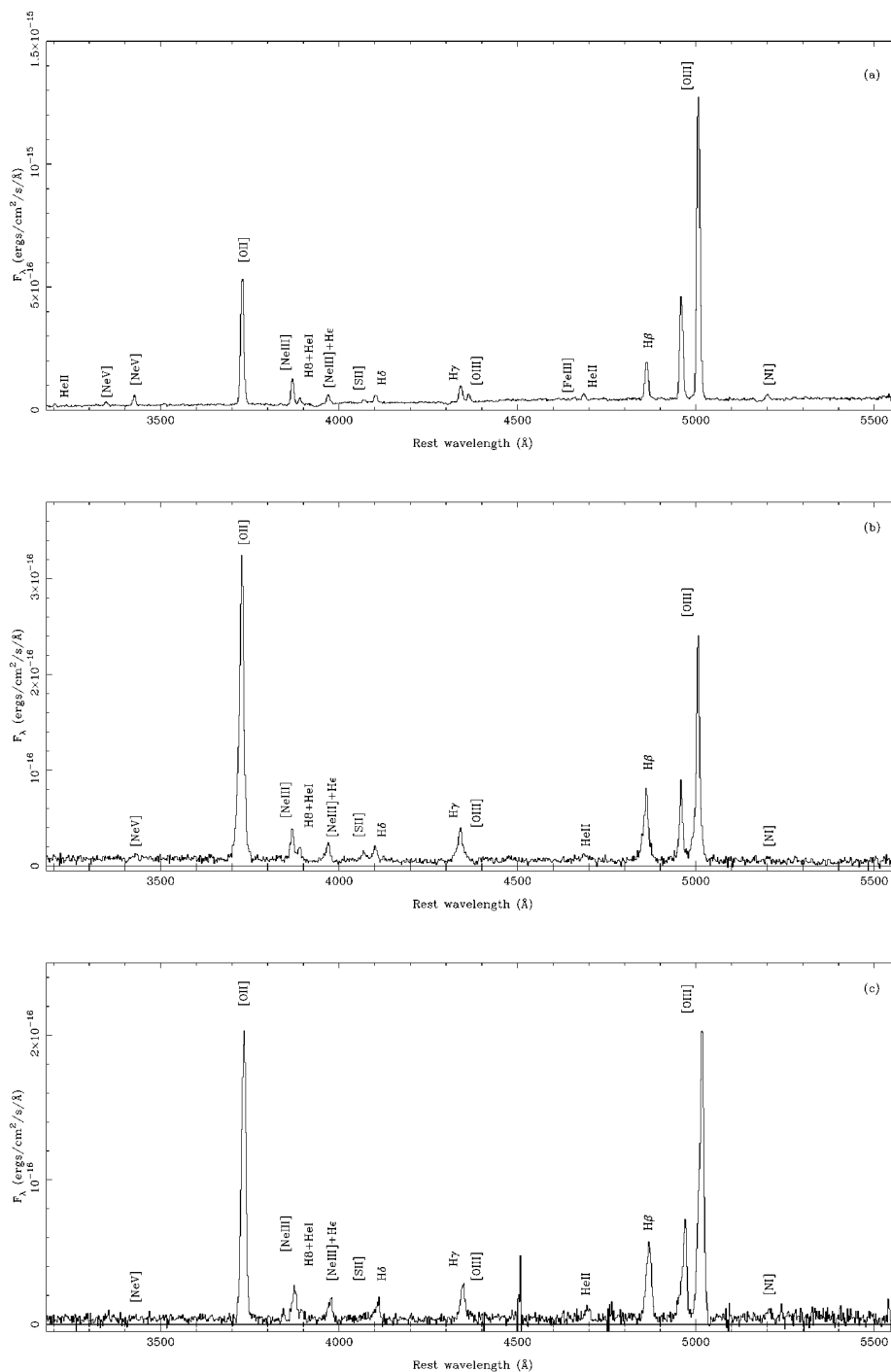


FIG. 10.—Spectra of (a) the central nuclear region ($1''.7 \times 1''.3$ aperture); (b) the eastern EELR ($3''.9 \times 1''.3$ aperture centered $3''.9$ east of the nucleus); and (c) the western EELR ($3''.9 \times 1''.3$ aperture centered $3''.9$ west of the nucleus), extracted from the blue low-dispersion long-slit spectrum. Some of the important emission lines are indicated.

was scaled by measuring the height of the 4000 \AA break for the blue data and the equivalent width of the stellar absorption lines for red data; the stellar subtraction has only a small effect on the measured line fluxes, owing to the large equivalent widths of the emission lines. The formal errors in the line fluxes from the Gaussian fitting procedure vary from approximately 1% for the strongest lines up to 40% for the weakest, blended lines.

It is clear that there is a large contrast in the ionization state of the emission-line gas between the nuclear region and the EELR. The changes in the ionization state are

clearly illustrated in Figures 12–13, which show the variations in the $[\text{O II}](3727)/[\text{O III}](5007)$, $[\text{O III}](5007)/\text{H}\beta$, and $[\text{O I}](6300)/[\text{O III}](5007)$ line ratios along the radio axis. In the nuclear region, the ionization state is observed to peak slightly east of the continuum centroid and then falls with increasing radius on either side of the nucleus. Pronounced minima in the ionization state are observed $\sim 4''.5$ east and $\sim 5''$ west of the nucleus, beyond which the ionization state is observed to rise again. The positions of the radio hot spots are also marked on these figures, which shows that *the minima in the mean ionization state of the extended line-*

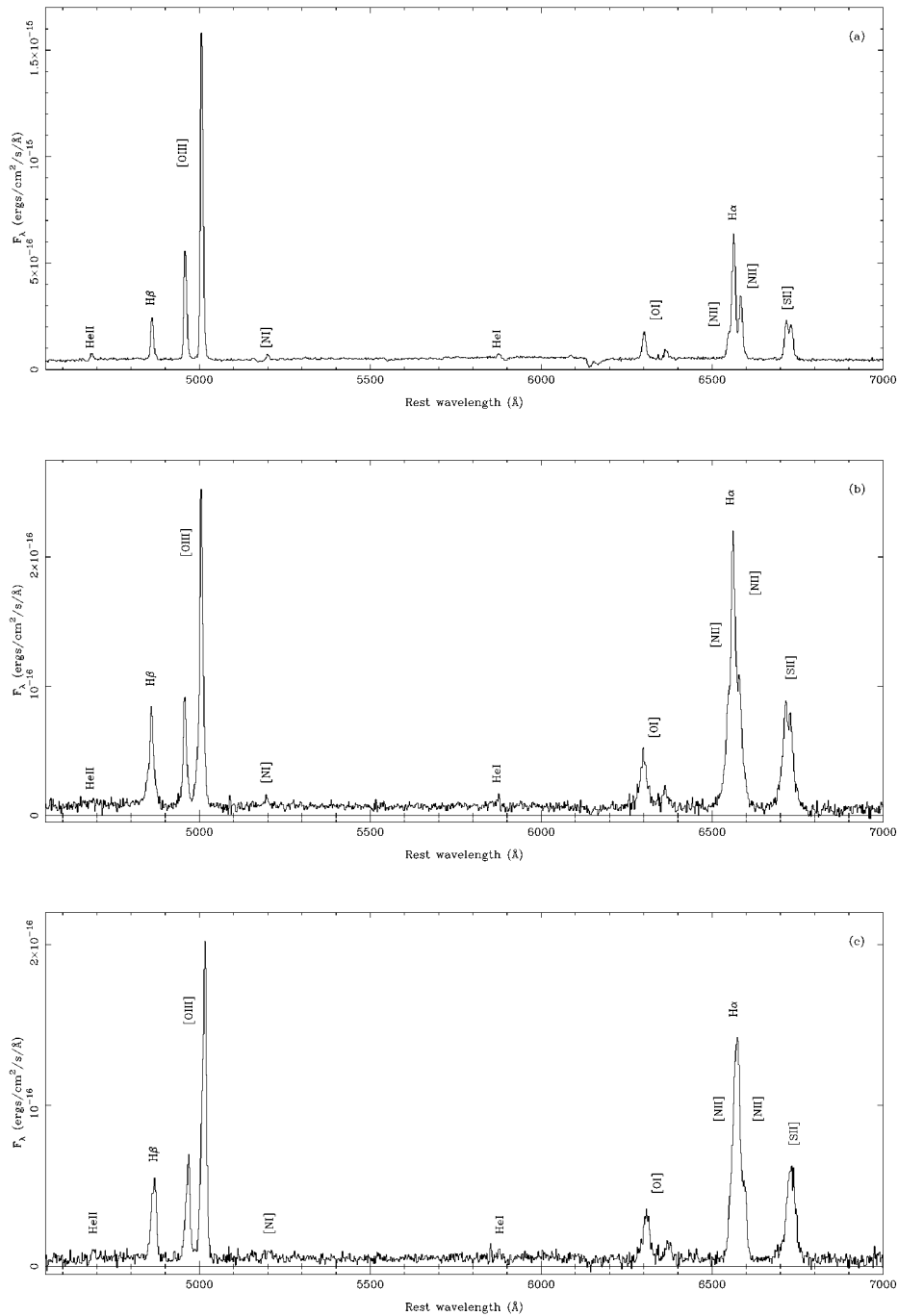


FIG. 11.—Spectra of (a) the central nuclear region; (b) the eastern EELR; and (c) the western EELR, extracted from the red low dispersion long-slit spectrum. Apertures as in Fig. 10.

emitting gas are closely associated with the hot spots on both sides of the nucleus.

It is important to emphasize that the results presented above were obtained by fitting single Gaussian profiles to the low-dispersion spectra, whereas we have seen from the high-dispersion spectra that the line emission originates in a number of discrete components, which need not necessarily—and indeed do not—emit line radiation with similar line ratios. So the results above give the “average” spectrum for the integrated line emission from several distinct components. From the high-resolution data it is possible to derive some information on the spectra and the ionization state of the different kinematic subcomponents,

which is clearly useful information if we are to learn more about the ionization mechanism and origin of these sub-systems.

The substantial change in the relative strengths of the various components at different positions along the radio axis is clearly illustrated in Figure 14, which shows the variation in the observed [O III] $\lambda 5007$ flux from each component. The broad low-ionization component appears to extend throughout the extended nebulosity, with a fall in surface brightness beyond the radio hot spot to the east, and beyond a radius of about $3''$ to the west. The lack of observed line emission from the central high-ionization component at a radius of $\sim 3''$ west of the nucleus is clear;

TABLE 4
EMISSION-LINE FLUXES MEASURED FROM THE BLUE LOW-DISPERSION LONG-SLIT SPECTRUM

| Wavelength (Å) | Line | Nucleus | E EELR | W EELR |
|--|-----------|---------|--------|--------|
| 3204 | He II | 0.03 | ... | ... |
| 3346 | [Ne V] | 0.08 | ... | ... |
| 3426 | [Ne V] | 0.22 | 0.04 | ... |
| 3727 | [O II] | 3.13 | 4.14 | 3.41 |
| 3865 | [Ne III] | 0.60 | 0.34 | 0.37 |
| 3886 | H8 + He I | 0.15 | 0.15 | 0.07 |
| 3967 | [Ne III] | 0.21 | 0.21 | 0.22 |
| 4071 | [S II] | 0.08 | 0.14 | 0.05 |
| 4102 | Hδ | 0.20 | 0.18 | 0.20 |
| 4340 | Hγ | 0.41 | 0.48 | 0.40 |
| 4363 | [O III] | 0.17 | 0.05 | 0.05 |
| 4658 | [Fe III] | 0.05 | ... | ... |
| 4686 | He II | 0.12 | 0.10 | 0.12 |
| 4861 | Hβ | 1.00 | 1.00 | 1.00 |
| 4959 | [O III] | 2.56 | 0.65 | 1.02 |
| 5007 | [O III] | 7.77 | 2.23 | 3.36 |
| 5199 | [N I] | 0.15 | 0.04 | 0.08 |
| Hβ flux (10 ⁻¹⁶ ergs cm ⁻² s ⁻¹) | | 22.2 | 14.1 | 11.1 |

the peak emission from the redshifted component occurs at the same location. The redshifted and blueshifted components are distributed symmetrically about the nucleus, peaking ~2".7 east and west of the core.

Typical values of the observed [O III](5007)/Hβ line ratio for each of the observed components are given in Table 3. The spectrum of the broad component is markedly different from the spectra of the narrower central component and the split components: it has a much lower ionization state, with $1 \leq [\text{O III}]/\text{H}\beta \leq 3$, whereas the narrower central component and the redshifted and blueshifted components have much higher ionization states, with $4 \leq [\text{O III}]/\text{H}\beta \leq 8$ generally. Any variation in the relative brightness of the broad component significantly affects the ionization of the integrated line emission. *The ionization minima observed on either side of the nucleus are due to peaks in the brightness of the low ionization broad component relative to the higher ionization components.*

The variation of the ionization state of the line-emitting gas with both velocity shift and displacement from the nucleus can also be studied in a model-independent manner. In order to do this, the contribution of the contin-

uum emission was first subtracted from the two-dimensional profiles of the [O III]λ5007 and Hβ emission lines in the blue high-dispersion long-slit spectra. The [O III] profile was then blueshifted by 145.52 Å to the wavelength of Hβ, and the ratio of the two profiles was computed. The derived two-dimensional variation of the [O III](5007)/Hβ ratio with velocity and position is shown in Figure 15 (Plate 24). The two-dimensional [O III]/Hβ variation confirms the results presented above that were derived by fitting Gaussians to the one-dimensional spectral line profiles. In particular, the broad low-ionization line emission, and the higher ionization emission from the central and shifted components, are all apparent in Figure 15.

4.5. Long-Slit Spectroscopy: The Physical Conditions

Accurate measurements of the electron temperature T_e from the temperature diagnostic line ratio [O III](5007 + 4959)/4363 were possible for the nucleus and the EELR. The mean values measured for this ratio from the low- and high-dispersion blue data are [O III](5007 + 4959)/4363 = 62 ± 4 , 40 ± 10 , and 70 ± 20 for the nucleus, the eastern EELR, and the western EELR,

TABLE 5
EMISSION-LINE FLUXES MEASURED FROM THE RED LOW-DISPERSION LONG-SLIT SPECTRUM

| Wavelength (Å) | Line | Nucleus | E EELR | W EELR |
|--|----------|---------|--------|--------|
| 4658 | [Fe III] | 0.05 | ... | ... |
| 4686 | He II | 0.14 | 0.04 | 0.08 |
| 4861 | Hβ | 1.00 | 1.00 | 1.00 |
| 4959 | [O III] | 2.60 | 0.82 | 1.05 |
| 5007 | [O III] | 7.89 | 2.67 | 3.35 |
| 5199 | [N I] | 0.11 | 0.07 | 0.09 |
| 5721 | [Fe VII] | 0.07 | ... | ... |
| 5755 | [N II] | 0.03 | 0.05 | ... |
| 5875 | He I | 0.10 | 0.08 | ... |
| 6086 | [Fe VII] | 0.06 | ... | ... |
| 6300 | [O I] | 0.83 | 0.87 | 0.76 |
| 6363 | [O I] | 0.25 | 0.25 | 0.22 |
| 6548 | [N II] | 0.68 | ... | ... |
| 6563 | Hα | 3.76 | 5.43 | 4.88 |
| 6583 | [N II] | 1.98 | ... | ... |
| 6717 | [S II] | 1.13 | 2.45 | 1.94 |
| 6731 | [S II] | 1.10 | ... | ... |
| Hβ flux (10 ⁻¹⁶ ergs cm ⁻² s ⁻¹) | | 19.8 | 14.9 | 12.1 |

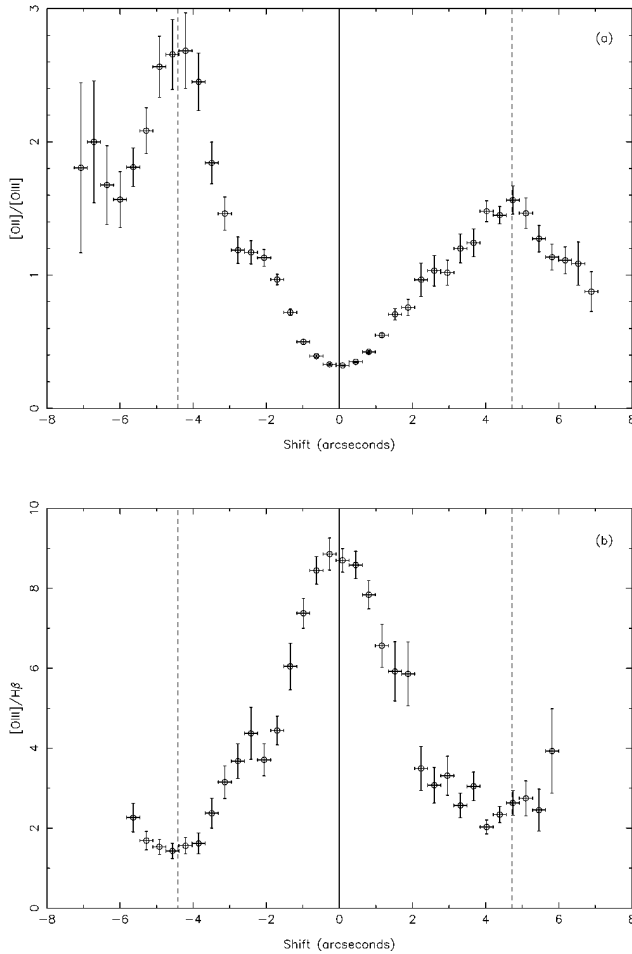


FIG. 12.—Variation in the ratios of strong emission lines along the radio axis from the blue low-dispersion spectrum: (a) $[O\ II](3727)/[O\ III](5007)$; (b) $[O\ III](5007)/H\beta$.

respectively, which indicates temperatures of $15,800^{+400}_{-500}$ K, $20,000^{+4000}_{-2000}$ K, and $15,000^{+3000}_{-2000}$ K. It was also possible to estimate the temperatures of the line-emitting gas in the nucleus and the eastern EELR using the line ratio $[N\ II](6548 + 6584/5755)$. The measured line ratios of 90 ± 20 and 70 ± 20 , respectively, imply $[N\ II]$ temperatures of 9800 ± 800 K and $13,000^{+4000}_{-2000}$ K. The significance of these electron temperatures is discussed in § 5.2.

From the $[S\ II](6717/6731)$ line ratio, a density measurement was also possible in the nuclear region: $[S\ II](6717/6731) = 1.20 \pm 0.02$, which implies a moderate density, $n_e = 270^{+30}_{-20} \text{ cm}^{-3}$. From the variation of this line ratio with radius, a central density peak can be seen coincident with the nuclear continuum centroid. In addition, there appears to be a small rise in the density (up to $\sim 500 \text{ cm}^{-3}$) approximately $1''$ either side of the nucleus, approximately corresponding to the projected positions of the inner filaments observed in the *HST* image. Unfortunately, owing to the complexity of the line profiles at larger radii, it is not possible to obtain reliable constraints on the electron density in the EELR from the $[S\ II]$ ratio.

4.6. Long-Slit Spectroscopy: The Continuum Emission

The spatial profile of the green continuum emission from 3C 171 is plotted in Figure 16. This profile is well fitted by a single Lorentzian profile that peaks in the same position as the nuclear line flux. There is a slight excess of continuum

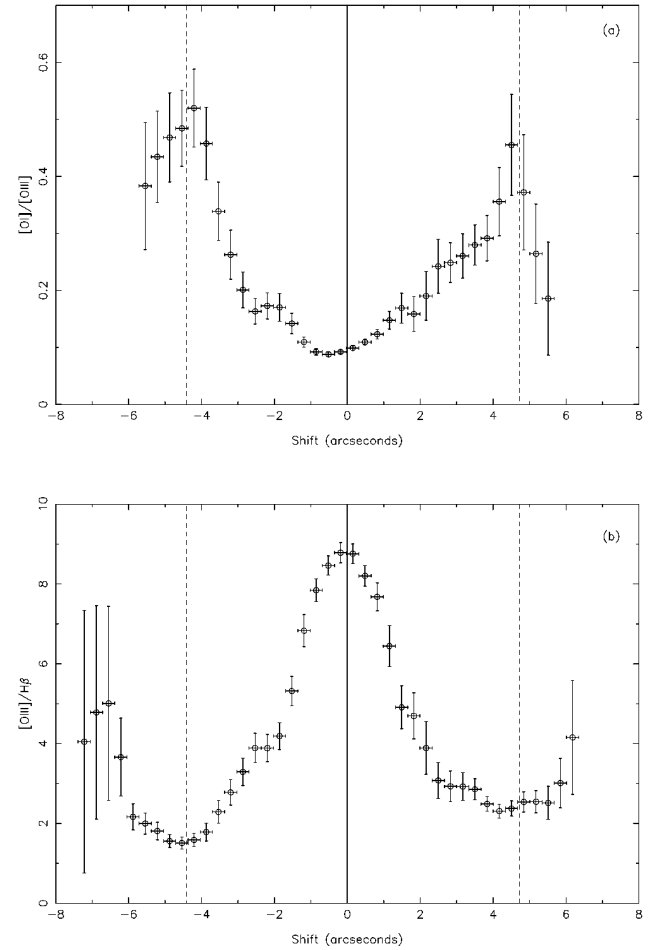


FIG. 13.—Variation in the ratios of strong emission lines along the radio axis from the red low-dispersion spectrum: (a) $[O\ I](6300)/[O\ III](5007)$; (b) $[O\ III](5007)/H\beta$.

emission observed approximately $4''$ east of the nucleus—this position is consistent with that of the foreground star seen in the *HST* image of 3C 171 (Fig. 2).

At shorter wavelengths, the continuum profile becomes highly distorted, with a strong peak associated with the

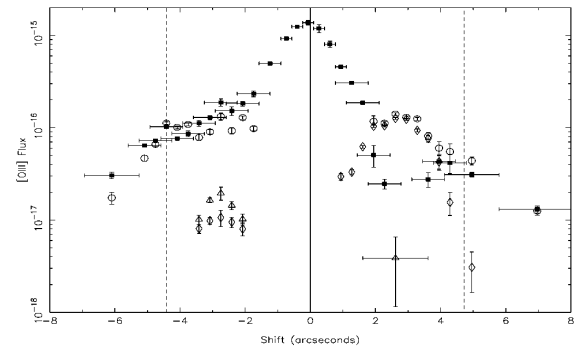


FIG. 14.—Variation in the $[O\ III] 45007$ line fluxes per pixel for the strongest line-emitting components, derived from multiple-Gaussian fits to the blue high-dispersion spectrum. The different components are as follows: broad central component (circles), narrow high-ionization component (filled squares), redshifted component (diamonds), and blueshifted component (triangles). The extraction apertures are plotted for the central high-ionization component, and the formal fitting errors are also plotted.

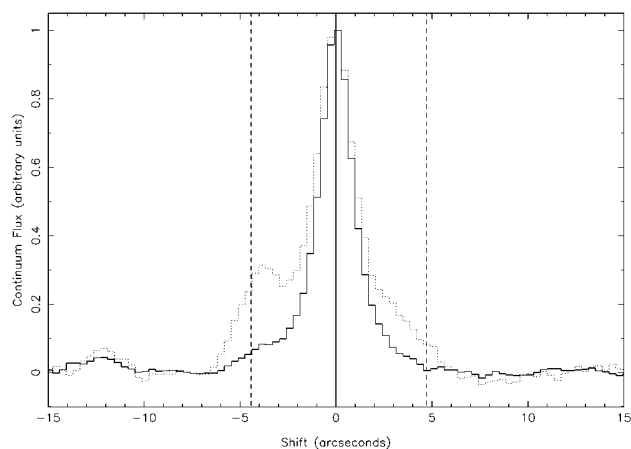


FIG. 16.—Profile of the line-free continuum emission along the radio axis, from the blue low-dispersion long-slit spectrum. The solid line shows the green continuum profile (5100–5500 Å), and the dotted line shows the profile at the UV end of the spectrum (3200–3700 Å).

eastern EELR and fainter extended continuum emission to the west (Fig. 16). An extended UV continuum excess was also observed in the long-slit spectra of H84. The aforementioned star is responsible for some of this excess continuum emission to the east, but this still leaves a substantial residual UV excess on either side of the nucleus.

As demonstrated by Dickson et al. (1995), the nebular continuum emission (a combination of Balmer, two-photon and free-free continua, plus higher order Balmer lines) can lead to strong UV continuum emission from radio galaxies wherever the emission lines have large equivalent widths. It is straightforward to calculate the theoretical contribution of the Case B nebular continuum from the measured $H\beta$ flux (see, e.g., Osterbrock 1989). The calculation is insensitive to density and temperature variations (for the range of physical conditions applicable to the EELR), and the only potential uncertainty is the differential reddening due to dust. As no significant reddening is measured in the spectra of 3C 171, this effect is not likely to be a problem.

Figure 17a shows a comparison between the continuum spectrum of the eastern EELR of 3C 171 and the nebular continuum emission derived using the Nebcont routine in DIPSO; the nebular-subtracted continuum spectrum is shown in Figure 17b (the higher order Balmer lines are not plotted). It is found that the nebular emission contributes $\sim 80\%$ of the continuum emission from the EELR below the Balmer break at 3646 Å. On nucleus, the continuum emission includes a stronger stellar contribution, but the nebular continuum is still significant in the nuclear region—particularly in the near-ultraviolet, where 30%–40% of the continuum emission is nebular. The rise in the equivalent width of the Balmer lines with increasing distance from the nucleus leads to an increase in the relative strength of the nebular continuum, and this is the cause of the blue continuum spectrum at large radii ($U-B \sim -0.6$ in the eastern EELR, compared with $+0.1$ in the nucleus) and of the distorted UV spatial profile. Figure 18 shows the observed spatial profile of the UV continuum emission for 3C 171 and the resulting profile after subtraction of the nebular continuum contribution. The nebular-subtracted continuum profile is not significantly different from the green continuum profile—which is dominated by starlight by the underlying host galaxy—except for a small remaining peak

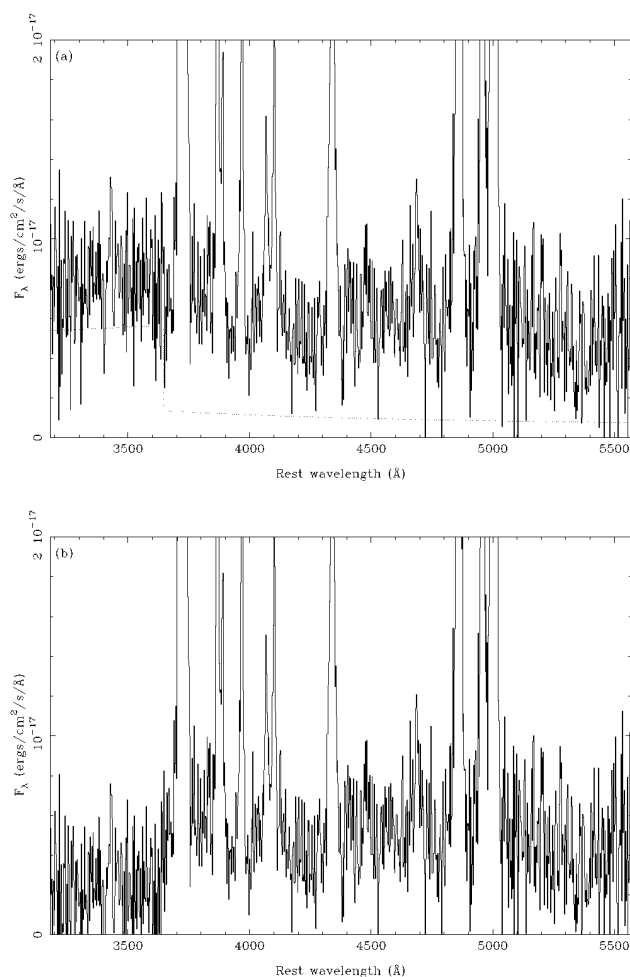


FIG. 17.—(a) Continuum spectrum of the Eastern EELR of 3C 171 ($2^{\circ}0-4^{\circ}0$ from the nuclear continuum centroid) from the blue low-dispersion long-slit spectrum, with the contribution from nebular continuum emission—calculated from the observed $H\beta$ flux using the NEBCONT routine in the DIPSO spectrum analysis package—superimposed (dotted line); (b) continuum spectrum of the EELR after subtraction of the nebular continuum contribution.

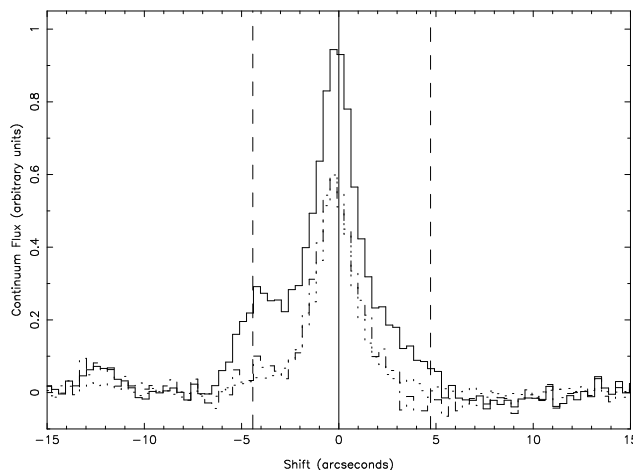


FIG. 18.—Continuum profile of 3C 171 derived from the blue low-dispersion data. The solid line indicates the observed near-UV continuum emission (3200–3700 Å), the dot-dashed line shows the UV continuum profile after subtraction of the nebular continuum emission (calculated from the $H\beta$ flux along the slit), and the dotted line shows the observed green continuum profile (5100–5500 Å, scaled to the peak of the nebular-subtracted blue profile).

in the eastern EELR, which is due to the star seen in the *HST* image. *There is no evidence for any residual UV continuum excess in 3C 171 after removal of the nebular continuum emission.* However, this does not rule out a substantial local source of ionizing photons from shock-heated clouds extending to EUV/X-ray wavelengths—see below.

The importance of the nebular continuum emission in powerful radio galaxies in general, particularly those at high redshifts, is discussed further in § 5.4.

5. DISCUSSION

In the following section, we summarize the evidence for shocks in 3C 171. The nature of the ionization mechanism(s) for the line-emitting gas is considered in § 5.2. In § 5.3, we compare 3C 171 with other low- to intermediate-redshift radio galaxies that show evidence for similar interactions. Finally, observations of high-redshift radio galaxies are discussed in § 5.4 and are compared with our results for 3C 171.

5.1. Evidence for Shocks in 3C 171

In this section we present the arguments that imply that the morphology, kinematics, and ionization structure of the extended ionized gas in 3C 171 are defined by shocks induced by strong jet-cloud interactions.

As was shown in § 4.1, the extended line emission in 3C 171 is closely aligned with the radio axis. This linear structure is likely to be caused by the lateral expansion of the jet cocoon, which sweeps up and shocks the ambient gas. Shocks along the length of the jet may also occur as a result of either clouds straying into the path of the jet or Kelvin-Helmholtz instabilities. In any case, the EELR morphology contrasts greatly with the broad “ionization cones” observed in several Seyfert galaxies (see, e.g., Tadhunter & Tsvetanov 1989). These features are believed to be due to photoionization of the otherwise undisturbed interstellar medium by ionizing radiation escaping from the AGN in a wide conical beam coaxial with an obscuring molecular torus. Orientation-based unified schemes for radio-loud AGNs (see, e.g., Barthel 1989) also require the presence of a molecular torus. However, the morphology and kinematics of the EELR in 3C 171 strongly suggest that it is not the result simply of photoionization of widely distributed interstellar gas by a conical radiation beam emanating from the nucleus but rather of an interaction between the radio jet and the ambient gas. Illumination of a gaseous envelope by relativistically beamed ionizing radiation could also produce a jetlike EELR aligned with the radio axis. Nevertheless, it remains necessary to explain why the radial extent of the line emission is similar to that of the radio source; the line fluxes fall steeply beyond radio lobes either side of the nucleus. The natural explanation for the morphology of the ENLR and its close association with the radio axis is that jet-induced shocks greatly enhance the brightness of the observed line emission. The exact mechanism is not immediately obvious. Shocks could act as effective local ionization sources, as discussed below. They could also increase the efficiency with which ionizing photons from the nucleus are reprocessed into line emission. In the latter case, the emission measure will increase as gas is swept up and compressed, or, alternatively, individual optically thick clouds might have their cross sections to ionizing radiation increased as they are first flattened and then shredded by the passage of the shock.

The radio structure is also related to the ionization structure of the EELR of 3C 171: minima in the $[\text{O III}]/\text{H}\beta$ ratio and maxima in the $[\text{O I}]/[\text{O III}]$ and $[\text{O II}]/[\text{O III}]$ ratios were shown in § 4.4 to be coincident with the eastern and western radio hot spots. One possible explanation for this close relationship between the ionization state and the radio structure is shock-induced density enhancement. Unfortunately, no direct density measurement was possible to check this hypothesis (§ 4.5), but a similar ionization minimum was observed associated with the radio hot spot in PKS 2250–41 (Clark et al. 1997), and in this case the high $[\text{S II}]$ density measured was shown to be consistent with shock-induced compression. Alternatively, local ionization may be important (§ 5.2). In either case, shocks are implicated.

The complex kinematical properties of the emission-line gas in 3C 171 were presented in § 4.3. It is first important to point out that the observed motions cannot be gravitational; such extreme, localized velocity shifts and line broadening must be the result of acceleration/turbulence induced by the passage of the radio jets through the ambient ISM. We now consider the origins of the various kinematic components (the broad low-ionization emission and the high-velocity split components observed on both sides of the nucleus).

One possible origin for the high-velocity split components seen in the high-dispersion spectra is ionized gas that has passed through the main bow shocks ahead of the radio jets. In this case, the displacement of $\sim 2''$ (10 kpc) behind the radio hot spots would represent a cooling length; it was similar displacements measured between the radio and optical emission in the NLR of Seyfert galaxies that prompted Pedlar, Unger, & Dyson (1985) and Taylor, Dyson, & Axon (1992) to propose the radio ejecta-driven bow shock model for Seyfert galaxies. However, in the radio maps of 3C 171—most clearly in recent high-resolution VLA maps (M. Hardcastle, private communication)—distinct knots/filaments of radio emission are evident at the inner edges of both radio lobes. These knots occur $\sim 2''.8$ east and west of the radio core and are therefore closely associated with the redshifted and blueshifted components observed in the high-dispersion spectra, which peak at similar positions both east and west of the nucleus (Fig. 14). This suggests that the split components are most likely due to jet-induced shocks at the positions of these radio knots, rather than earlier interactions with the strong shocks at the head of the eastern and western radio jets. The highest surface brightness extended features seen in the broadband *HST* images—the large knot of emission to the east of the nucleus, and the brightest part of the filament to the west—are also spatially associated with the radio knots and the split emission-line components. A further argument against the cooling length explanation is that the radio-optical displacement is larger to the west, whereas the larger line widths and higher $[\text{O III}]$ temperature indicate that the shock speed is highest in the eastern EELR.

Any model of the jet-cloud interactions in 3C 171 must explain the observed anticorrelation between the line widths and the ionization state. A similar phenomenon has also been observed in the powerful radio galaxy PKS 2250–41 (Clark et al. 1997) and also in shocked supernova remnants (Shull 1983) and in numerical simulations of bow shocks (Taylor et al. 1992). The high-dispersion spectra of 3C 171 indicate that this anticorrelation is due to the fact

that the line emission contains contributions from both low ionization-state gas ($[\text{O III}]/\text{H}\beta \sim 2$) with a broad velocity distribution ($\text{FWHM} \sim 1000 \text{ km s}^{-1}$) and relatively high ionization gas ($[\text{O III}]/\text{H}\beta \sim 5$) with a much narrower velocity distribution ($\text{FWHM} \sim 200 \text{ km s}^{-1}$).

The natural interpretation of the observed decrease in ionization state with increasing velocity dispersion is that the density of the line-emitting gas increases with velocity dispersion. This can be explained by the compression effect of fast shocks, as follows. The warm clouds of gas will be subjected to shocks with a range of velocities (due to the spread of shock velocities across the surface of the bow shock, differing initial cloud densities, etc.). As the compression factor of an isobaric shock is proportional to the square of the shock velocity (to first order), we would therefore expect to find a spread of final cloud densities, with an anticorrelation between density and line width. Photoionized precursor gas may contribute to the narrow, high ionization-line emission, and large-scale turbulence (seen in the numerical simulations of de Young 1986) or the breakup of individual emission-line clouds behind the bow shock (produced by the shocked-cloud models of Klein, McKee, & Colella 1994) could contribute to the broad-line emission. In any case, it is difficult to conceive of a situation in which this anticorrelation would be observed without shocks. Although the ionizing photons could come from either the shock front or the AGN, strong shocks must be involved and can themselves be effective ionization sources.

5.2. Ionization of the Line-emitting Gas

In the previous section, it was demonstrated that shocks are important in the EELR of 3C 171, which raises the possibility of an important role for shock ionization. In this

section, we consider the ionization mechanism in more detail by comparing the observed line ratios with the predictions of photoionization and shock-ionization models.

In Figure 19, the variation in the ratios of several strong, unblended lines measured along the radio axis of 3C 171 $\{[\text{O II}](3727)/[\text{O III}](5007), [\text{O I}](6300)/[\text{O III}](5007), \text{ and } [\text{O III}](5007)/\text{H}\beta\}$ are plotted on diagnostic diagrams. The pixel-by-pixel variation in the line ratios along the slit reveals how the relative strengths of different lines, and the corresponding ionization state of the warm gas, vary along the radio axis. More important, it may also give an indication of how the ionization mechanism changes with radius.

Within the region $\sim 1''.6$ (19 kpc) on either side of the nucleus, the ionization state falls steadily as the radius increases. The observations fall directly on the $\alpha = -1.5$ power-law photoionization curve on the plot of $[\text{O III}](5007)/\text{H}\beta$ against $[\text{O II}](3727)/[\text{O III}](5007)$ and just below it on the plot of $[\text{O III}](5007)/\text{H}\beta$ against $[\text{O I}](6300)/[\text{O III}](5007)$. This supports the notion that the inner line emission is from gas that is photoionized by a central, geometrically diluted, AGN continuum source. The observations in this inner region are inconsistent with the models for the other continuum spectra plotted ($\alpha = -1.0$ and -2.0), in agreement with the result of Robinson et al. (1987) that only power-law spectra ionizing spectra with $-1.75 < \alpha < -1.25$ are consistent with the line ratios measured in a sample of low-redshift radio galaxies, whereas for the general population of radio galaxies, we see a sequence in this diagram—indicative of a trend in the ionization parameter—for 3C 171 the individual line-emitting regions form a similar trend.

Beyond a radius of $\sim 3''.6$ there is a slight break in the $[\text{O III}](5007)/\text{H}\beta$ ratio, and the agreement of the obser-

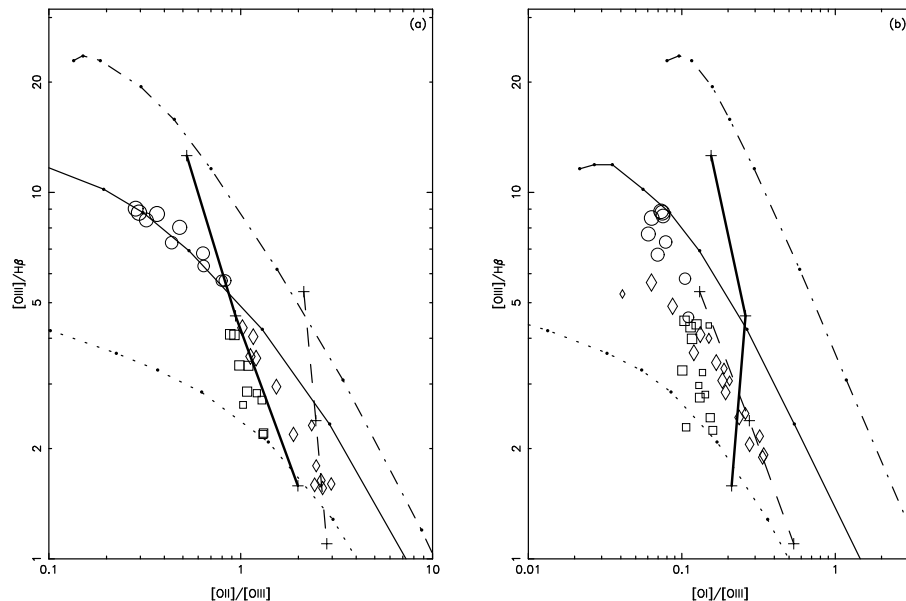


FIG. 19.—Diagnostic diagram showing the pixel-by-pixel variation in the following line ratios (derived from single Gaussian fits to the line profiles) along the radio axis of 3C 171: (a) $[\text{O III}](5007)/\text{H}\beta$ against $[\text{O II}](3727)/[\text{O III}](5007)$, from the blue low-dispersion long-slit spectrum; and (b) $[\text{O III}](5007)/\text{H}\beta$ against $[\text{O I}](6300)/[\text{O III}](5007)$, from the red low-dispersion long-slit spectrum. The circles denote the nuclear region, and the open diamonds and squares represent points more than $1''.5$ east and west of the core, respectively. The sizes of the symbols are proportional to the $[\text{O III}](5007)$ fluxes measured for each pixel. The crosses linked by a dashed line and a thick solid line indicate the predictions of the fast shock models of Binette et al. (1985) and Dopita & Sutherland (1995); going from top to bottom, the crosses represent shock velocities of (116, 131, 212 km s^{-1}) and (500, 300, 200 km s^{-1}) for the Binette et al. (1985) and Dopita & Sutherland (1995) models, respectively. The circles linked by dotted, solid, and dot-dashed lines represent the line ratios produced by optically thick single-slab power-law photoionization models ($f_{\nu} \propto \nu^{\alpha}$) with spectral indices of $\alpha = -1.0, -1.5$, and -2.0 , respectively (Robinson et al. 1987); going from top left to bottom right, the circles represent ionization parameters of ($10^{-1}, 5 \times 10^{-2}, 2.5 \times 10^{-2}, 10^{-2}, 5 \times 10^{-3}, 2.5 \times 10^{-3}, 10^{-3}, 5 \times 10^{-4}, 2.5 \times 10^{-4}, \text{ and } 10^{-4}$).

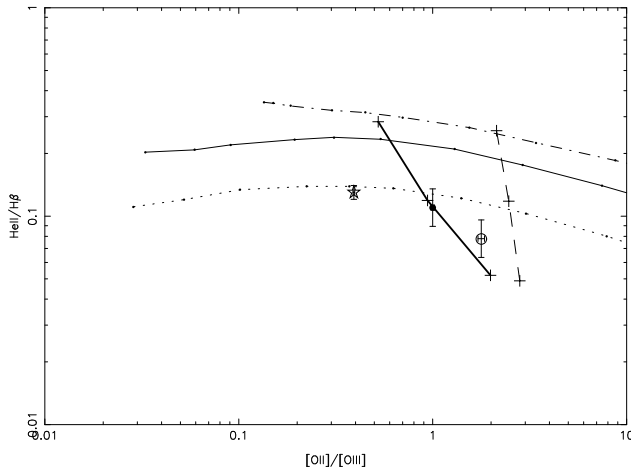


FIG. 20.—Line ratio diagnostic diagram showing the He II(4686)/H β line ratio plotted against [O II](3727)/[O III](5007), with 1 σ error bars (from the blue low-dispersion spectrum). The star denotes the nuclear region of 3C 171 (1"7 \times 1"3 aperture), and the hollow and filled circles represent the extended line-emitting gas 2"–6" east and west of the nucleus, respectively. The symbols representing the shock and photoionization models are as in Fig. 19.

variations with the $\alpha = -1.5$ photoionization model appears to break down. The observations fall consistently below and to the left of this model in both the eastern and western EELR; a steeper continuum slope produces better agreement with some of the data points, although it is difficult to explain the line ratios observed in both the eastern and the western EELR with the same ionizing continuum spectrum. Unfortunately, it is not possible to investigate the detailed trends in the line ratio variations along the radio axis for other strong lines {[S II](6717 + 6731)/H α , [N II](6583 + 6548)/H α etc.} because of the severe blending of the complex line profiles.

The He II(4686)/H β line ratios measured in the nuclear and extended regions of 3C 171 present major problems for AGN photoionization models: the He II emission is much weaker in the extended gas than is predicted by the $\alpha = -1.5$ power-law photoionization model (Fig. 20). For photoionization, the He II/H β ratio is a strong discriminant of the "hardness" of the ionizing continuum—more specifically the fraction of ionizing photons with energies above 4 ryd (Robinson et al. 1987; Binette, Robinson, & Courvoisier 1988). This is clearly illustrated in Figure 20, in which the model predictions are plotted for power-law continua with spectral indices $\alpha = -1.0$, -1.5 and -2.0 , which shows the clear dependence of He II/H β on α (and the lack of variation with ionization parameter U). Although the steeper $\alpha = -2.0$ ionizing spectrum can reproduce the weak He II λ 4686 emission observed in the EELR, this does not solve the problem because the other observed line ratios are generally inconsistent with such steep ionizing spectra, particularly in the nuclear region.⁶ The [Ne V] λ 3426 emission is also much weaker in the EELR of 3C 171 (but not in the nucleus) than predicted by photoionization models.

The final line ratio that causes problems for photoionization models is the electron temperature diagnostic line ratio [O III](5007 + 4959)/4363. As was discussed in § 4.5, this

ratio has been measured in the extended and nuclear line-emitting regions of 3C 171. The values obtained are much lower than the photoionization models predict. In the nucleus, this can be attributed to collisional suppression of the [O III] λ 4959, 5007 lines—which have lower critical densities than the [O III] λ 4363 line—but since this explanation requires densities higher than 10^5 cm^{-3} , it cannot apply in the EELR. The derived electron temperatures are in the range $15,000 \leq T_e \leq 21,000 \text{ K}$, whereas photoionization generally leads to electron temperatures $T_e \leq 11,000 \text{ K}$; high [O III] temperatures have also been measured in the extended line-emitting gas observed around other radio galaxies (Tadhunter, Robinson, & Morganti 1989).

It is important to emphasize that the photoionization models discussed above are single-slab models. Recently, more complex two-phase photoionization models have been presented that can produce a spread in the He II(4686)/H β and [O III](5007 + 4959)/4363 line ratios (Binette et al. 1996; Simpson & Ward 1996). However, these models do not produce temperatures as high as are measured in the EELR of 3C 171; they also predict an increase in the [O III] temperature with increasing ionization state and He II/H β ratio, whereas we observe the opposite effect.

Summarizing the above, it appears from examination of the optical line ratios measured in the EELR (and to a lesser extent the nucleus) of 3C 171 that AGN photoionization fails to explain certain key features of the emission-line spectra. In view of the clear evidence presented above for jet-cloud interactions in the EELR, an obvious alternative is heating and ionization by jet-induced shocks. To assess the importance of shock ionization in the EELR, it is necessary to consider how well the predictions of shock models compare with the observed line ratios. Models of fast shocks applicable to the conditions in the EELR of radio galaxies have been studied by several authors (Binette, Dopita, & Tuohy 1985; Sutherland et al. 1993; Dopita & Sutherland 1995, 1996). These models include the effects of ionizing radiation from the hot shocked gas on both the upstream precursor gas and the cooled gas downstream.

Shocks are complex nonequilibrium systems, and the output spectrum is very sensitive to a number of parameters, making it difficult to make detailed comparisons between the observations and the model predictions. However, a low He II/H β ratio and a high [O III] temperature are a common feature of shock models with shock velocities up to $\sim 300 \text{ km s}^{-1}$. These velocities may seem low, considering that the range of velocities measured in the eastern EELR of 3C 171 is $\sim 2500 \text{ km s}^{-1}$ (FWZI). However, the velocities observed in the ionized gas do not necessarily measure the actual shock velocities in the clouds. From pressure balance arguments, the shock velocities in the warm clouds are of the order of 30 times lower than the shock velocity in the hot ISM. Although the warm clouds of gas are initially accelerated as they pass through the shock front to a velocity of the order of the shock speed within the cloud, the cloud velocities will increase as they are dragged along by the faster moving hot ISM gas (Klein et al. 1994).

The low He II(4686)/H β ratios measured in the EELR of 3C 171 provide some of the strongest evidence that the extended line emission is predominantly ionized by shocks. As discussed above, the shock models of Binette et al. (1985) and Dopita & Sutherland (1995, 1996) with velocities up to $\sim 300 \text{ km s}^{-1}$ predict He II λ 4686 strengths that are consis-

⁶ A low He II/H β ratio appears to be characteristic of EELR that harbor strong shocks (Clark 1996), which is further evidence that this phenomenon is a result of the shocks rather than an unusually steep AGN continuum.

tent with those observed (Fig. 20). The high [O III] temperatures in the extended gas are also in agreement with the agreement of shock models (they arise because much of the [O III] emission comes from shock-heated gas that is cooling from $T_e \sim 30,000$ K), as are the low [Ne V] $\lambda 3426$ fluxes measured in the EELR (Dopita & Sutherland 1995). The ratios of the other strong emission lines observed in the EELR of 3C 171 (such as [O III]/H β , [O II]/[O III], etc.) also agree with these shock models (Fig. 19). The detailed variation of the line ratios in the EELR are not well reproduced by the models plotted, but this is not surprising as they are simple, one-phase, single-velocity plane-parallel shocks that do not take into account the structure of the bow shock. It is also possible that the locus of points on the diagnostic diagrams may reflect the variation in the relative importance of AGN photoionization versus shock ionization, with a steady increase in the contribution from shock ionization as the radio hot spots are approached. What is important is that *shock models with shock velocities of a few hundred kilometers per second are broadly consistent with the line ratios measured in the EELR of 3C 171, including the He II/H β and [O III] (5007 + 4959)/4363 ratios (which are not reproduced by the photoionization models)*.

The situation is less clear-cut in the central nuclear region. The fact that a low He II/H β ratio is measured here may indicate that shock ionization is also important closer to the central AGN. Further evidence for shocks in the nucleus of 3C 171 is provided by the inner aligned filaments seen in the *HST* image. However, the shock models of Binette et al. (1985) and Dopita & Sutherland (1995) cannot simultaneously reproduce the low He II/H β ratio and the [O II]/[O III], [O I]/[O III] and [O III]/H β ratios measured in the vicinity of the nucleus.

As discussed in § 4.4, the variation in the ionization state of the integrated emission is partly due to changes in the relative strength of the emission from the different kinematic components, so that for completeness it is necessary to consider these components separately. With this in mind, diagnostic diagrams for the different kinematic components are shown in Figure 21 for several extraction apertures where fits to the strong components are reasonably well constrained for all lines. It seems from Figure 21 that the central narrow component on both sides of the nucleus and the redshifted component to the west occupy similar positions on the diagnostic diagrams. The line ratios for the nuclear region are similar, but with a slightly higher ionization state. The data for all of these components are generally consistent with the $\alpha = -1.5$ power-law photoionization model. In contrast, the broad component has a much lower ionization state (as discussed in § 4.3), and the line ratios of this component are consistent with the shock models of Binette et al. (1985) and Dopita & Sutherland (1995). However, this diagram must be treated with caution—by isolating distinct kinematical components, we may be selecting different zones in the shock structure, whereas the models treat only the integrated line emission.

It was stated in § 4.6 that there is no significant UV excess detected in the EELR of 3C 171. In view of the evidence for shock ionization presented above, it may seem surprising that there is no sign of the necessary ionizing radiation. However, by comparing the observational upper limit on the UV flux at 3500 Å from the EELR of 3C 171 with the continuum energy distributions for shocked plasmas tabulated by Dopita & Sutherland (1996), we estimate an upper

limit on the ionizing luminosity of 10^{45} ergs s $^{-1}$ (neglecting attenuation), which is 2 orders of magnitude higher than the total emission-line luminosity estimated from the line fluxes observed in the EELR; equivalently, the H β equivalent widths measured in the EELR are orders of magnitude lower than those produced by the shock models. Consequently, photoionization by UV photons from hot shocked gas is still a viable ionization mechanism.

In summary, there is a strong case for believing that the EELR in 3C 171 is associated with strong shocks driven by the radio jet. There is also evidence that shocks contribute significantly to the ionization of the line-emitting gas near the radio hot spots, but the precise balance between this and photoionization by the AGN radiation field is difficult to determine. At low ionization parameters, it has been shown (Villar-Martin, Tadhunter, & Clark 1997) that UV line ratios provide a method of distinguishing between shock ionization and AGN photoionization. For this reason, UV spectroscopy of 3C 171 is required in order to determine unambiguously the ionization mechanism of the extended line-emitting gas.

5.3. Comparison with Other Nearby Radio Galaxies

The strikingly similar properties of the EELR observed in 3C 171 and another powerful intermediate-redshift radio galaxy PKS 2250–41 (Tadhunter et al. 1994; Clark et al. 1997) have been mentioned briefly above; in this section, the comparison between these two sources is considered in more detail. In addition, we also discuss the possible parallels between these two sources and the less powerful nearby ($z = 0.0462$) radio galaxy IRAS 04210+0400 (Hill, Wynn-Williams, & Becklin 1988; Holloway et al. 1996).

Some of the properties shared by 3C 171 and PKS 2250–41 are (1) a close spatial association between the radio and optical emission-line structures; (2) an anticorrelation between ionization state and line width; (3) a low ionization state in the extended gas and ionization minima associated with the radio hot spots; and (4) low He II/H β ratios and high [O III] temperatures. The properties common to the two sources have been interpreted as the result of fast shocks in the extended gas (Clark 1996). The total radio and emission-line luminosities are also similar in the two sources, and both lie at intermediate redshifts.

The major differences between these sources are (1) the emission-line morphologies—while the extended line emission in 3C 171 has a linear structure extended along the radio axis between the radio hot spots, the main EELR in PKS 2250–41 has a bow-shock morphology and circumscribes the western radio hot spot (with fainter arcs to the east); (2) radio morphologies—the radio emission from PKS 2250–41 has a simple double-lobed structure typical of powerful FR II radio galaxies, in contrast to the highly disturbed morphology of 3C 171; (3) the kinematics are more extreme in 3C 171—this is mainly due to the line splitting at the inner radio knots, and if these features are ignored, the velocity shifts and line widths are similar in the two sources.

A blue continuum source beyond the western radio lobe in PKS 2250–41 also distinguishes the two sources. This is believed to be associated with a companion galaxy with which the radio jet is colliding, and this may hold the key to the other differences listed above. In PKS 2250–41, the bright line-emitting arc is apparently the result of shocks driven by the violent interaction between the radio jet and

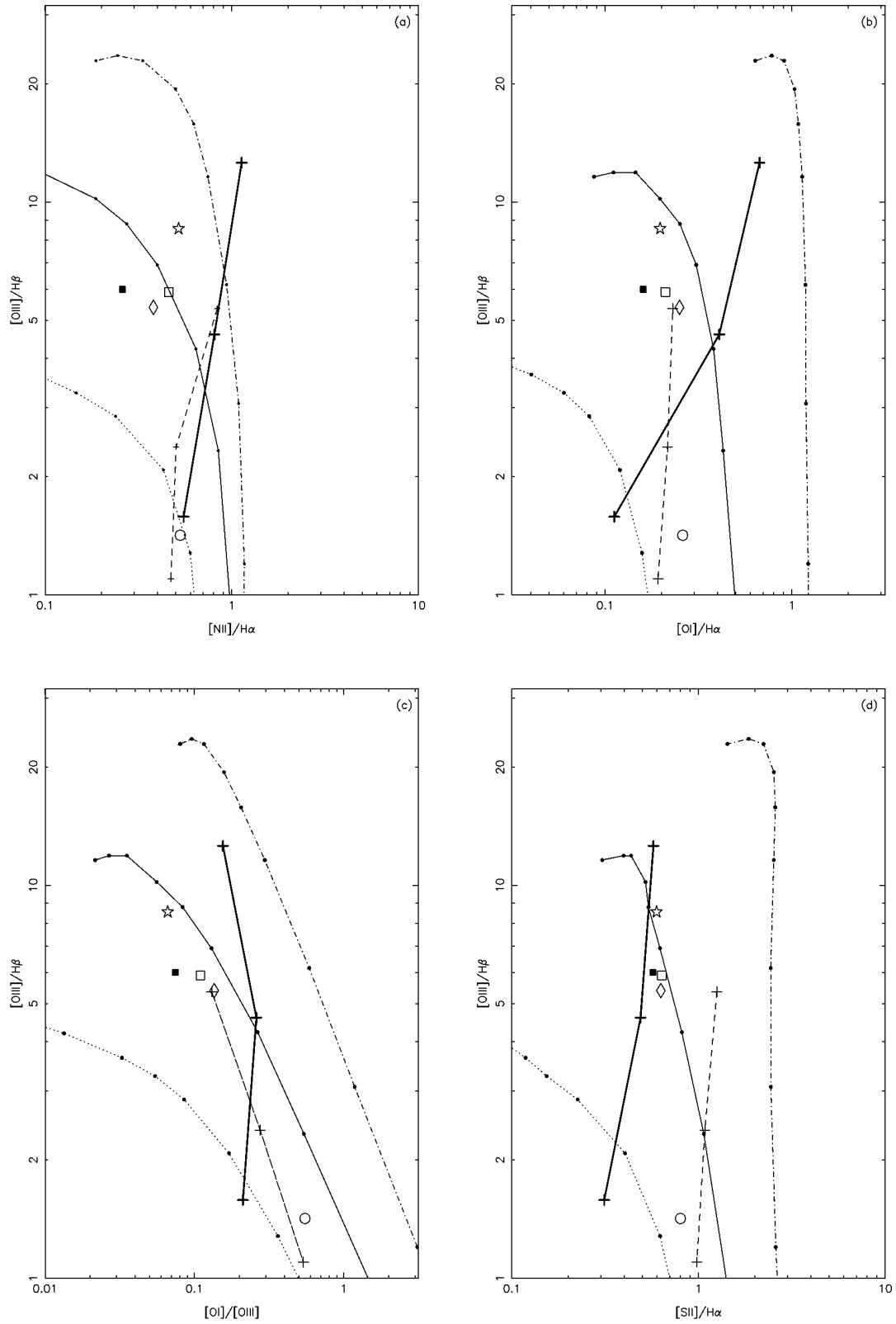


FIG. 21.—Line ratio diagnostic diagrams for the different kinematic components seen in 3C 171, in the nuclear region and the eastern and western EELR, derived from the red and blue high-dispersion data. The line ratios plotted are $[O\text{ III}](5007)/H\beta$ against (a) $[N\text{ II}](6583)/H\alpha$; (b) $[O\text{ I}](6300)/[O\text{ III}](5007)$; (c) $[O\text{ I}](6300)/H\alpha$; and (d) $[S\text{ II}](6717 + 6731)/H\alpha$. The symbols representing the observational data are as follows: star, integrated nuclear emission, $2''.4$ aperture; circle, broad central component, $3''.7$ to $7''.0$ arcseconds east of the core; filled square, narrow central component, $3''.7$ – $7''.0$ east of the core; diamond, redshifted component, $1''.0$ – $2''.4$ west of the core; open square, narrow central component, $1''.0$ – $2''.4$ west of the core. The symbols representing the shock and photoionization models are as in Fig. 19.

the companion galaxy. In contrast, no other galaxies are observed within ~ 60 kpc of 3C 171: the EELR morphology in 3C 171 is consistent with a more even ISM distribution, with shocks being important along the length of the radio axis. Both the ionization minima and the peak in line flux are closer to the nucleus (relative to the working surfaces of the radio jets) in 3C 171 than in PKS 2250–41, as would be expected for more distributed shocks.

IRAS 04210+0400 is another source that shows similarities with 3C 171: (1) the radio lobes expand perpendicular to the radio axis beyond the hot spots; (2) the emission-line gas is distributed in a collimated jetlike structure along the radio axis; (3) the line width of the gas increases at the radio hot spots, and there is an anticorrelation between line width and ionization state; and (4) there is an ionization minimum associated with the hot spots. In this source, it is clear that the radio source flares suddenly beyond the radio hot spots. Holloway et al. (1996) suggest that this is because there is a sudden drop in ambient density, which causes the jet flow to expand rapidly with a large opening angle. Ambient gas is entrained, which results in the observed kinematically disturbed line emission.

The many similarities suggest that a similar phenomenon may be occurring in 3C 171: a sudden drop in external pressure as the radio jets propagate beyond the confines of the host galaxy, which causes the radio plasma to expand at its internal sound speed and entrains clouds of warm gas that are observed in line emission. This is certainly a possible model—the end result is still the shocking of warm gas clouds along the radio axis, as has been considered throughout this paper. However, there are other possible explanations, and it is important to bear in mind that although the radio and optical structures of PKS 2250–41 are very different from those seen in 3C 171 (and IRAS 04210+0400), these radio galaxies are very similar in most other respects.

It is interesting to note at this point that both jetlike and arclike distributions of line-emitting gas have been observed in recent *HST* images of the NLR of Seyfert galaxies (Bower et al. 1994; Capetti et al. 1996). As with the radio galaxies discussed above, the emission-line jets are coincident with the associated linear radio sources, whereas the arcs lie at the outer edges of the hot spots. This structural dichotomy has been interpreted as being due to shocks along the length of and at the head of the small-scale radio jets, respectively (Capetti et al. 1996). The kinematics of the NLR are also affected by shocks as in the radio galaxy EELR, and there is some evidence for shock ionization (although shock ionization is likely to be relatively less important in Seyfert galaxies, owing to the lower power of the radio jets and the intensity of the ionizing radiation from the nearby AGNs).

5.4. Jet-Cloud Interactions in High-Redshift Radio Galaxies

The powerful radio galaxies observed at high redshift exhibit many of the properties observed in 3C 171, including luminous line emission extending along the radio axis, with the maximum line intensities often occurring off nucleus (McCarthy, Spinrad & van Breugel 1995; McCarthy et al. 1996); close associations between the extended line emission and distinct radio components (Djorgovski et al. 1987; Miley et al. 1992; Longair et al. 1995); aligned UV continuum emission (McCarthy et al. 1987; Chambers et al. 1987); and extreme line widths and

velocity shifts (Chambers, Miley & van Breugel 1990; McCarthy et al. 1996). There is overwhelming evidence that the EELR in 3C 171 is associated with a violent jet-cloud interaction; interstellar gas is accelerated and compressed by shocks induced by the radio jet, and the brightness of its line emission thereby greatly enhanced. The many common features shared by more distant powerful radio galaxies strongly suggests that jet-cloud interactions are also important at higher redshifts. It is important to note that the radio luminosities of radio galaxies at $z > 1$ are a couple of orders of magnitude higher than that of 3C 171—assuming that the jet mechanical energy increases with radio power, this implies that shocks will have an even greater influence on the kinematics and morphology of the line-emitting gas in these sources. However, the detailed evolution of both the AGN luminosity and the jet mechanical energy with radio power is not known, and therefore how the balance between AGN photoionization and shock ionization will change with redshift is also unclear.

The details of the emission-line spectra and the physical conditions in the radio galaxies observed at high redshifts are not well constrained, mainly because many important diagnostic lines are shifted into the infrared. However, the ionization state of the extended line-emitting gas appears to be low in many of these sources (e.g., 3C 368: Djorgovski et al. 1987; 3C 356: Lacy & Rawlings 1994) as in 3C 171, consistent with an increased contribution from low ionization state shocked gas in the more distant sources. A recent study of a sample of distant radio galaxies (Villar-Martin et al. 1997) found that the UV line ratios were inconsistent with both the AGN photoionization models and the shock models that fitted the optical line ratios at lower redshifts. Subsolar abundances are the most likely reason for this, but again the relative importance of shocks and AGN photoionization is uncertain.

The structures observed in recent *HST* images of powerful $z \sim 1$ radio galaxies (Best, Longair, & Rottgering 1996) indicate an apparent evolution in the structure of the extended optical/UV emission with radio size, which is most simply interpreted as being due to an age effect. Best et al. (1996) argue that the evolution from elongated, multimodal morphologies to smaller, rounder emission distributions as the radio source expands is due to jet-induced star formation followed by ordinary passive evolution of the stars. However, while the broadband images do not allow a detailed investigation of the emission mechanism, the known strength of the line emission in these sources indicates that both nebular continuum and line emission must make major contributions to the observed structures; in particular, the extended UV continuum emission in 3C 368 is known to be dominated by nebular continuum emission (see below). In the case of 3C 171, we find no evidence whatsoever of jet-induced star formation: the EELR line ratios are indicative of a “hard” ionizing continuum rather than a starburst; there are no spectral signatures of hot stars; and the extended continuum is almost nebular. Bearing this in mind, the evolution in the optical morphologies of powerful radio galaxies can be explained by jet-cloud interactions without recourse to jet-induced star formation. The passage of the jet through the ambient ISM sweeps up, compresses, disrupts, heats, and ionizes the warm gas. While the jet is passing through the dense halo of the galaxy, intense aligned line emission is observed, owing to both local ionization and the increase in covering factor

caused by the interaction with the gas clouds. As the source evolves, the radio jet expands out of the galactic halo, and the emission-line surface brightness falls off at large radii (the ambient gas density falls off rapidly, and therefore the emission measure falls and the cooling times increase until they are greater than the Hubble time). The bright aligned line emission closer to the central AGN will also fade with time, because (1) the local source of ionization provided by the shocks is no longer present (although shocks may occur along the length of the radio jets, the strongest shocks will be at the head of the jet); and (2) the shocked clouds of gas along the radio axis will disperse with time and may eventually be destroyed owing to the high velocities and turbulence induced by the shocks.

Consider the example of the powerful high-redshift radio galaxy 3C 368 ($z = 1.132$), which is often considered the archetypal high-redshift radio galaxy. Figure 22 (Plate 25) compares broadband *HST* images of 3C 368 and 3C 171. There is a striking similarity between the optical structures (the aligned filaments and knots) observed in the two sources. The relative positions of the radio hot spots and the optical line/continuum emission are also similar in 3C 368 and in 3C 171. The most noticeable difference in the morphologies is that the stellar emission from the halo of the host galaxy is relatively strong in 3C 171 because (1) 3C 368 is imaged in the rest-frame UV where stellar emission is weak; and (2) 3C 368 is a more powerful source, and therefore the line and nebular continuum emission are much stronger.

Recently, spectroscopic observations of 3C 368 have been obtained with the Keck telescope (Stockton, Ridgway, & Kellogg 1996), and again there is a striking resemblance with our spectra of 3C 171. First, the measured Balmer line strengths imply that, as for 3C 171, the off-nuclear UV continuum emission is dominated by nebular continuum emission (confirming the results of Dickson et al. 1995). The ionization levels in the extended line-emitting gas are similarly low (the $[\text{O II}](3727)/\text{H}\gamma$ ratio is 8.3 for the integrated EELR emission from both sources), and the level of ionization falls off nucleus in both sources. The detailed kinematic structures of the line-emitting gas are also similar: in both 3C 171 and 3C 368, a central narrow component is observed extending the length of the nebulosities with a smooth and relatively small change in velocity. Superimposed on this component are the split components (most clearly resolved in 3C 171) and the broad diffuse emission.

Summarizing the above discussion, the numerous similarities between 3C 171 and 3C 368—together with the spectroscopic evidence for shocks in 3C 171 presented in this paper—suggests that shocks play a crucial role in 3C 368. In addition to the similarities between 3C 171 and 3C 368, an examination of the Keck long-slit spectrum reveals more direct evidence for shocks in 3C 368. A faint, narrow, high ionization state line-emitting component is observed extending $\sim 2''$ – $6''$ north of the nucleus, which clearly represents line emission from gas that has not been subjected to the shocks driven by the expanding radio jet. The striking contrast between the properties of this component and those of the EELR associated with the radio jet are immediately apparent: (1) kinematics—the full width zero maximum of the $[\text{O II}]$ profile for the precursor gas and the shocked gas are $< 100 \text{ km s}^{-1}$ and $> 1000 \text{ km s}^{-1}$ respec-

tively; (2) ionization state—the precursor gas has a much higher ionization state than the extended line emission from the shocked gas ($[\text{O II}]/[\text{Ne V}] = 3$ for the precursor, compared to ~ 50 for the diffuse shocked gas); (3) surface brightness—the emission-line surface brightness of the northern knot is over 100 times higher than that of the undisturbed precursor gas. These observations are entirely consistent with the properties of the bright aligned emission being defined by the acceleration, compression, and ionization effects of strong shocks.

Thus, the observations of 3C 368 demonstrate the crucial role of shocks in high redshift radio galaxies; detailed studies of relatively nearby shocked sources such as 3C 171 are therefore important if we are to understand the physics of distant radio galaxies.

6. CONCLUSIONS

We have presented observations of the extended emission line region (EELR) associated with the powerful radio galaxy 3C 171. These observations probe the intimate relationship between the radio and optical line emission, which we interpret as being the result of shocks induced by jet-cloud interactions. There is compelling evidence that the distribution, kinematics, and physical conditions of the extended line-emitting gas in 3C 171 are defined by shocks. The evidence for ionization by fast shocks in 3C 171 (the low $\text{He II}/\text{H}\beta$ ratios and high $[\text{O III}]$ temperatures) is suggestive, but AGN photoionization remains a possibility. UV spectroscopy of this source is necessary in order to determine unambiguously the ionization mechanism of the extended gas.

A blue continuum excess is apparent along the radio axis of 3C 171. This has been shown to be dominated by nebular continuum emission from the line-emitting gas—there is no evidence for jet-induced star formation in this source.

In future papers (Clark et al. 1998), detailed studies will be presented of two further radio galaxies that show clear evidence for shocks. A subsequent discussion paper will draw the results of these studies together and consider in detail the far-reaching implications for radio galaxies in general and high-redshift radio galaxies in particular. We note here that the many similarities between 3C 171 and more distant sources such as 3C 368 imply that shocks play a crucial role in high redshift radio galaxies.

This paper is based largely on work carried out by the LAG (Lovers of Active Galaxies) collaboration. LAG is a consortium of mainly European astronomers that was established to study active galaxies using the International Time allocation at the Canary Islands' observatories operated under the auspices of the Comité Científico Internacional. The William Herschel Telescope is operated by the Royal Greenwich Observatory at the Roque de los Muchachos of the Instituto de Astrofísica de Canarias. We are grateful to the UK PPARC Starlink Project for providing the FIGARO data reduction software and computing facilities. N. E. C. acknowledges financial from ESA in the form of an ESA Fellowship, and earlier support from the University of Sheffield and PPARC. The authors are grateful to Katherine Blundell for generously providing us with the radio map of 3C 171 presented in this paper.

REFERENCES

- Barthel, P. D. 1989, *ApJ*, 336, 606
- Baum, S. A., Heckman, T. M., Bridle, A., van Breugel, W. J. M., & Miley, G. K. 1988, *ApJS*, 68, 643
- Baum, S. A., Heckman, T. M., & van Breugel, W. J. M. 1992, *ApJ*, 389, 208
- Best, P. N., Longair, M. S., & Rottgering, H. J. A. 1996, *MNRAS*, 280, L9
- Binette, L., Dopita, M. A., & Tuohy, I. R. 1985, *ApJ*, 297, 476
- Binette, L., Robinson, A., & Courvoisier, T. J.-L. 1988, *A&A*, 190, 29
- Binette, L., Wilson, A. S., & Storchi-Bergmann, T. 1996, *A&A*, 312, 365
- Blundell K. 1994, Ph.D. thesis, Univ. of Cambridge
- . 1996, *MNRAS*, 283, 538
- Bower, G. A., Wilson, A. S., Mulchaey, J. S., Miley, G. K., Heckman, T. M., & Krolik, J. H. 1994, *AJ*, 107, 1686
- Bruzual A., G., & Charlot, S. 1993, *ApJ*, 405, 538
- Burstein, D., & Heiles, C. 1982, *AJ*, 87, 1165
- Capetti, A., Axon, D. J., Macchetto, F., Sparks, W. B., & Boksenberg, A. 1996, *ApJ*, 469, 554
- Chambers, K. C., Miley, G. K., & van Breugel, W. J. M. 1987, *Nature*, 329, 604
- . 1990, *ApJ*, 363, 21
- Clark, N. E. 1996, Ph.D. thesis, Univ. of Sheffield
- Clark, N. E., Tadhunter, C. N., Morganti, R., Killeen, N. E. B., Fosbury, R. A. E., Hook, R. N., & Shaw, M. 1997, *MNRAS*, 286, 558
- Clark, N. E., et al. 1998, in preparation
- de Kopf, S., Baum, S. A., Sparks, W. B., Biretta, J., Columbek, D., Macchetto, F., McCarthy, P. J., Miley, G. K. 1996, *ApJS*, 107, 621
- de Young, D. S. 1981, *Nature*, 293, 43
- . 1986, *ApJ*, 307, 62
- Dickson, R., Tadhunter, C. N., Shaw, M. A., Clark, N. E., & Morganti, R. 1995, *MNRAS*, 273, L29
- Djorgovski, S., Spinrad, H., Pedelty, J., Rudnick, L., & Stockton, A. 1987, *AJ*, 93, 6
- Dopita, M. A., & Sutherland, R. S. 1995, *ApJ*, 455, 468
- , R. S. 1996, *ApJS*, 102, 161
- Fosbury, R. A. E. 1989, in *ESO Workshop on Extranuclear Activity in Galaxies*, ed. E. J. A. Meurs & R. A. E. Fosbury (Garching: ESO), 169
- Heckman, T. M., van Breugel, W. J. M., & Miley, G. K. 1984, *ApJ*, 286, 509
- Hill, G. J., Wynn-Williams, C. G., & Becklin, E. E. 1988, *ApJ*, 335, 93
- Holloway, A. J., Steffen, W., Pedlar, A., Axon, D. J., Dyson, J. E., Meaburn, J., & Tadhunter, C. N. 1996, *MNRAS*, 279, 171
- Klein, R., McKee, C., & Colella, P. 1994, *ApJ*, 420, 213
- Kuhr, H., Nauber, U., Pauliny-Toth, I. I. K., & Witzel, A. 1979, *A Catalogue of Radio Sources* (Bonn: Max-Planck Institut für Radio Astronomie)
- Lacy, M., & Rawlings, S. 1994, *MNRAS*, 270, 431
- Longair, M. S., Best, P. N., & Rottgering, H. J. A. 1995, *MNRAS*, 275, L47
- McCarthy, P. J. 1988, Ph.D. thesis, Univ. of California, Berkeley
- McCarthy, P. J., Baum, S., & Spinrad, H. 1996, *ApJS*, 106, 281
- McCarthy, P. J., Spinrad, H., & van Breugel, W. J. M. 1995, *ApJS*, 99, 27
- McCarthy, P. J., van Breugel, W. J. M., Spinrad, H., & Djorgovski, S. 1987, *ApJ*, 321, L29
- Meisenheimer, K., & Hippelein, H. 1992, *A&A*, 264, 455
- Miley, G. K., Chambers, K. C., van Breugel, W. J. M., & Macchetto, F. 1992, *ApJ*, 401, L69
- Osterbrock, D. E. 1989, *The Astrophysics of Gaseous Nebulae and Active Galactic Nuclei* (Mill Valley: University Science)
- Pedlar, A., Unger, S. W., & Dyson, J. E. 1985, *MNRAS*, 214, 463
- Rigler, M. A., Lilly, S. J., Stockton, A., Hammer, F., & Le Fèvre, O. 1992, *ApJ*, 385, 61
- Robinson, A., Binette, L., Fosbury, R. A. E., & Tadhunter, C. N. 1987, *MNRAS*, 227, 97
- Rowan-Robinson, M., Hughes, J., Jones, M., Leech, K., Veda, K., & Walker, D. W. 1991, *MNRAS*, 249, 729
- Shull, P. 1983, *ApJ*, 275, 611
- Simpson, C., & Ward, M. 1996, *MNRAS*, 282, 797
- Stockton, A., Ridgway, S. E., & Kellogg, M. 1996, *AJ*, 112, 902
- Sutherland, R. S., Bicknell, G. V., & Dopita, M. A. 1993, *ApJ*, 414, 510
- Tadhunter, C. N., Fosbury, R. A. E., & Quinn, P. 1989, *MNRAS*, 240, 225
- Tadhunter, C. N., Robinson, A., & Morganti, R. 1989, in *Extranuclear Activity in Galaxies*, ed. R. A. E. Fosbury & E. J. A. Meurs (Garching: ESO), 293
- Tadhunter, C. N., Shaw, M. A., Clark, N. E., & Morganti, R. 1994, *A&A*, 288, L21
- Tadhunter, C. N., & Tsvetanov, Z. I. 1989, *Nature*, 341, 422
- Taylor, D., Dyson, J. E., & Axon, D. J. 1992, *MNRAS*, 255, 351
- van Breugel, W. J. M., Heckman, T. M., Miley, G. K., & Filippenko, A. 1986, *ApJ*, 311, 58
- van Breugel, W. J. M., Miley, G. K., Heckman, T. H., Butcher, H. R., & Bridle, A. H. 1985, *ApJ*, 290, 496
- van Ojik, R. 1995, Ph.D. thesis, Leiden Obs.
- Véron, X., & Véron-Cetty, X. 1993, *A Catalogue of Quasars and Active Nuclei* (6th ed.; Garching: ESO)
- Villar-Martin, M., Tadhunter, C. N., & Clark, N. E. 1997, *A&A*, 323, 21

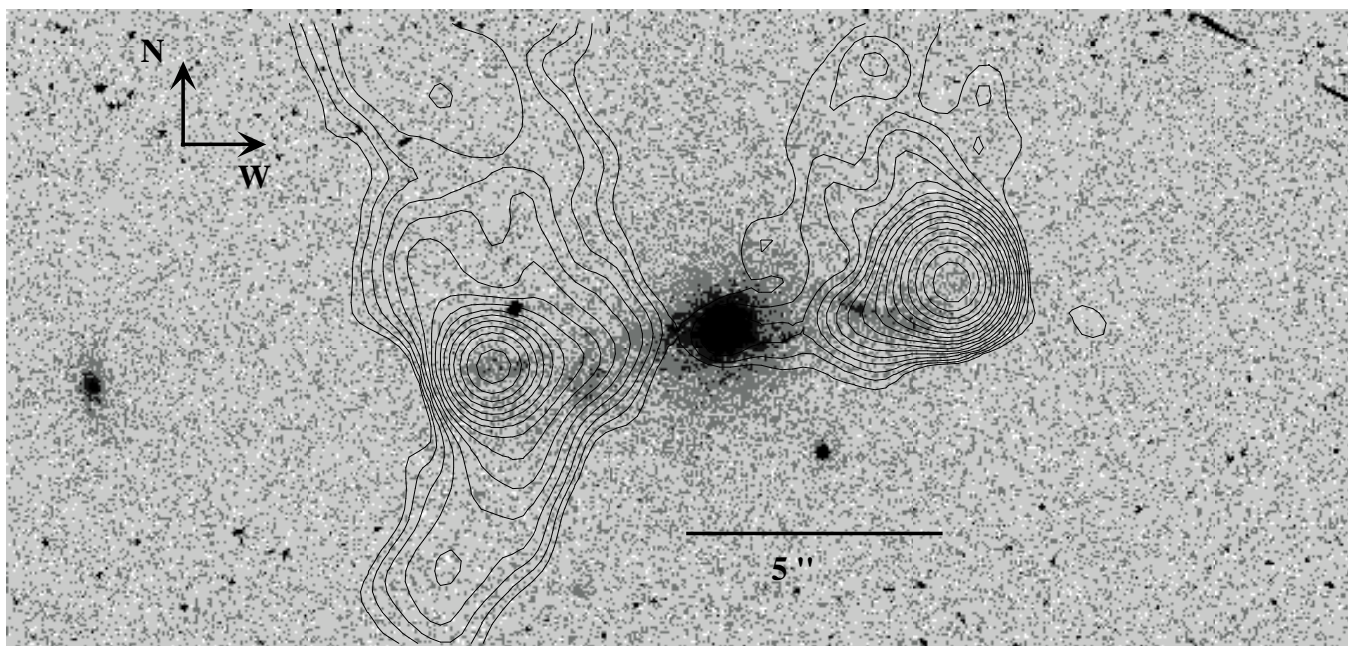
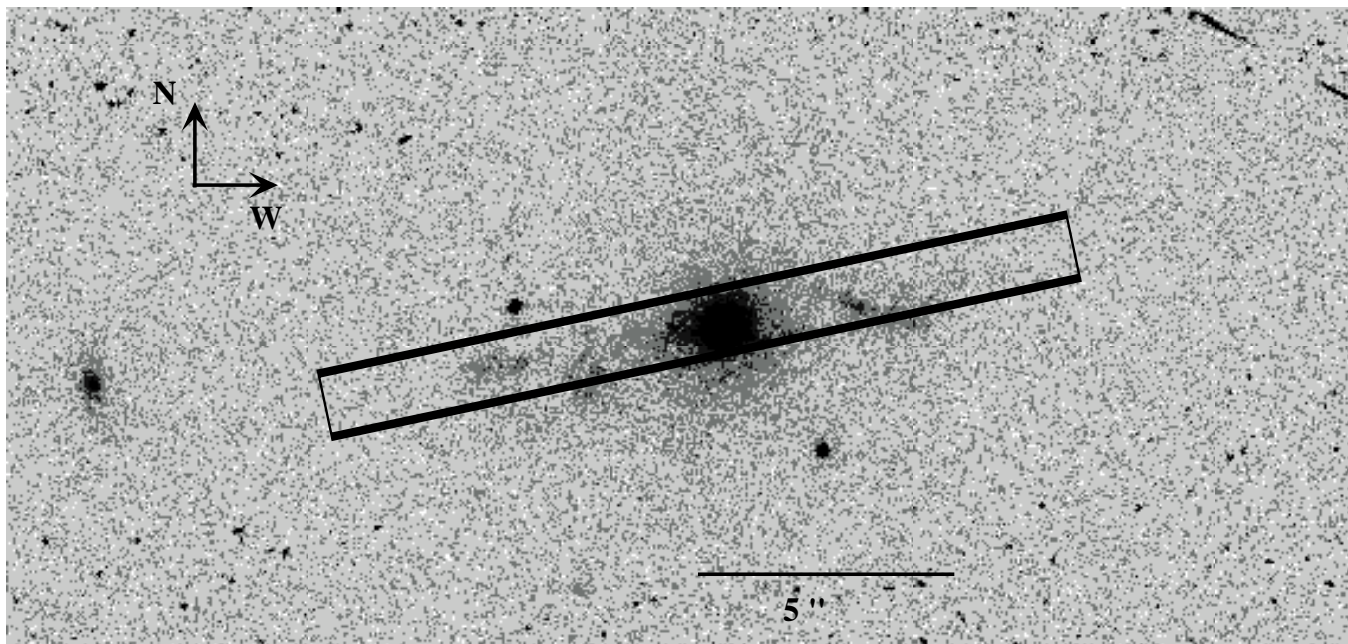


FIG. 2.—Gray-scale representation of the broadband WFPC2 *HST* image of 3C 171 (resolution $0''.1$). Superimposed on this image are the projected position of the slit used for our long-slit spectroscopy (*top*); and contours of the 8 GHz VLA radio map (*bottom*; resolution $1''$). Scale and orientation are as indicated.

CLARK ET AL. (see 494, 548)

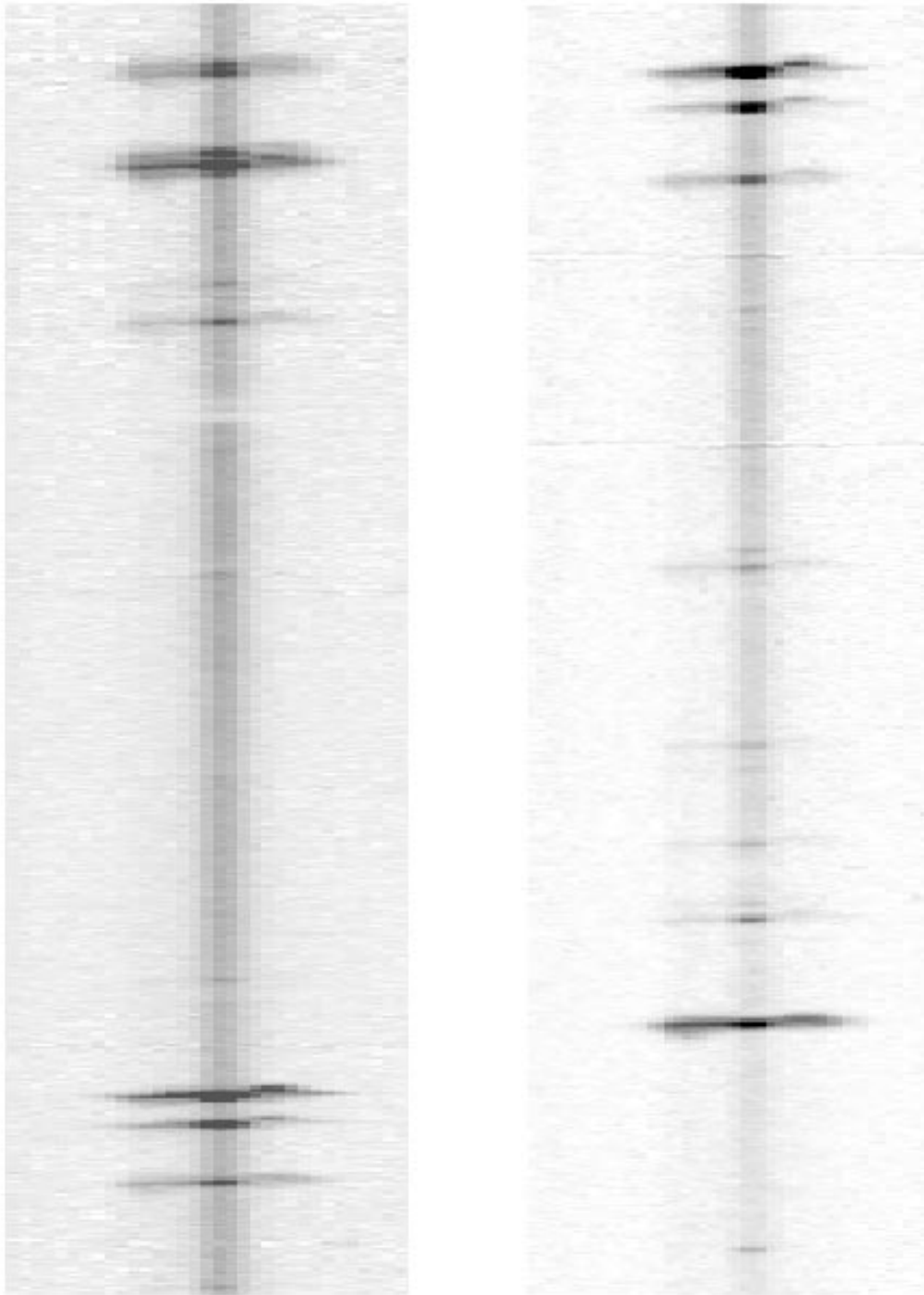


FIG. 3.—Gray-scale representations of the low-dispersion long-slit spectra of 3C 171: the red spectrum (*left*), with lines from $H\beta$ to $[S\ II]\ \lambda 6731$; the blue spectrum (*right*), extending from $[Ne\ V]\ \lambda 3426$ to $[O\ III]\ \lambda 5007$. West is to the right; wavelength increases to the top.

CLARK ET AL. (see 494, 549)

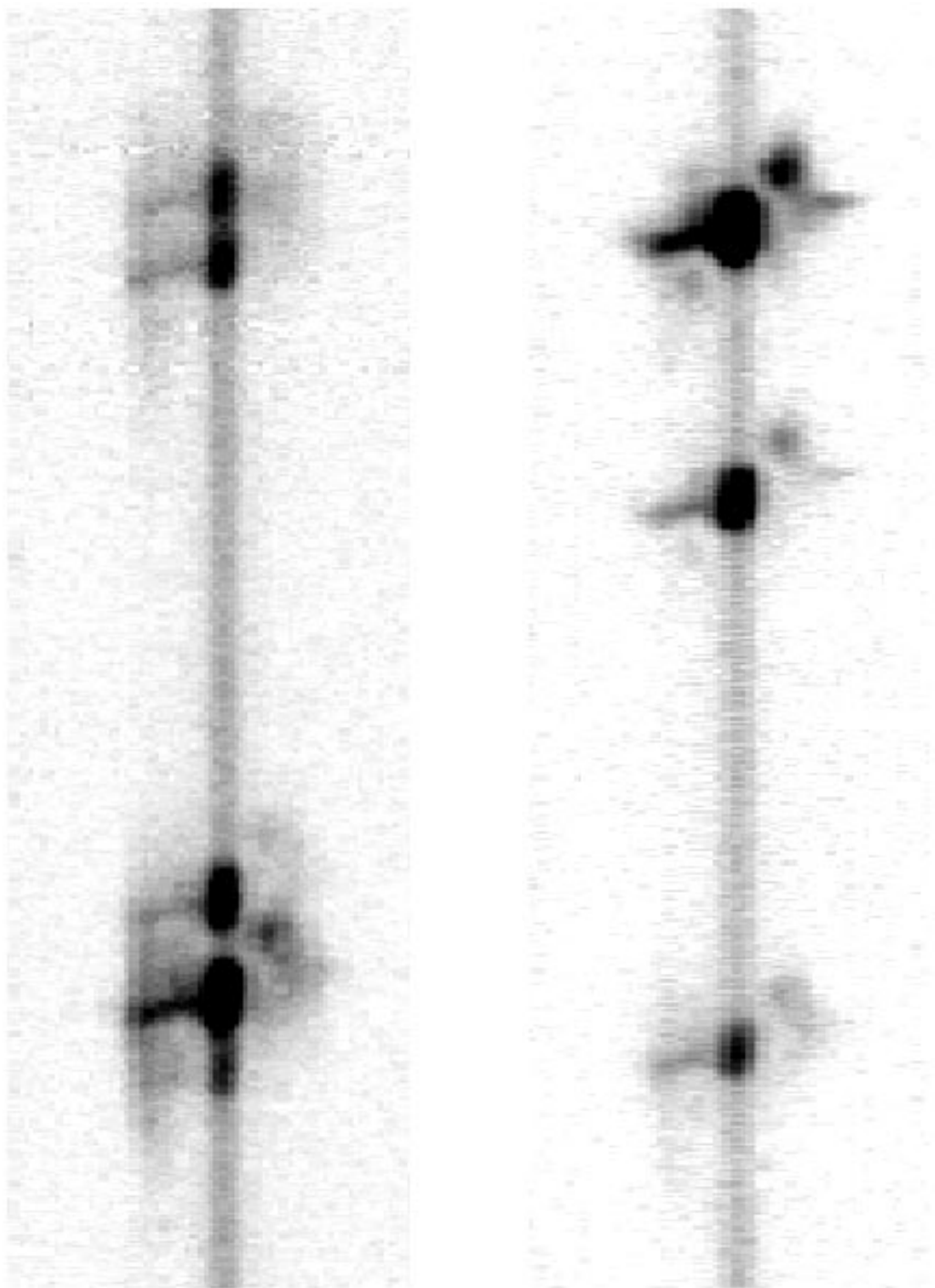


FIG. 4.—Gray-scale representations of the high dispersion long-slit spectra of 3C 171: the red spectrum (*left*), including the emission lines $H\alpha$, $[N\ II]\ \lambda\lambda 6548, 6583$ and $[S\ II]\ \lambda\lambda 6717, 6731$; the blue spectrum (*right*), showing the $H\beta$ and $[O\ III]\ \lambda\lambda 4959, 5007$ emission lines. Orientation as in Fig. 3.

CLARK ET AL. (see 494, 549)

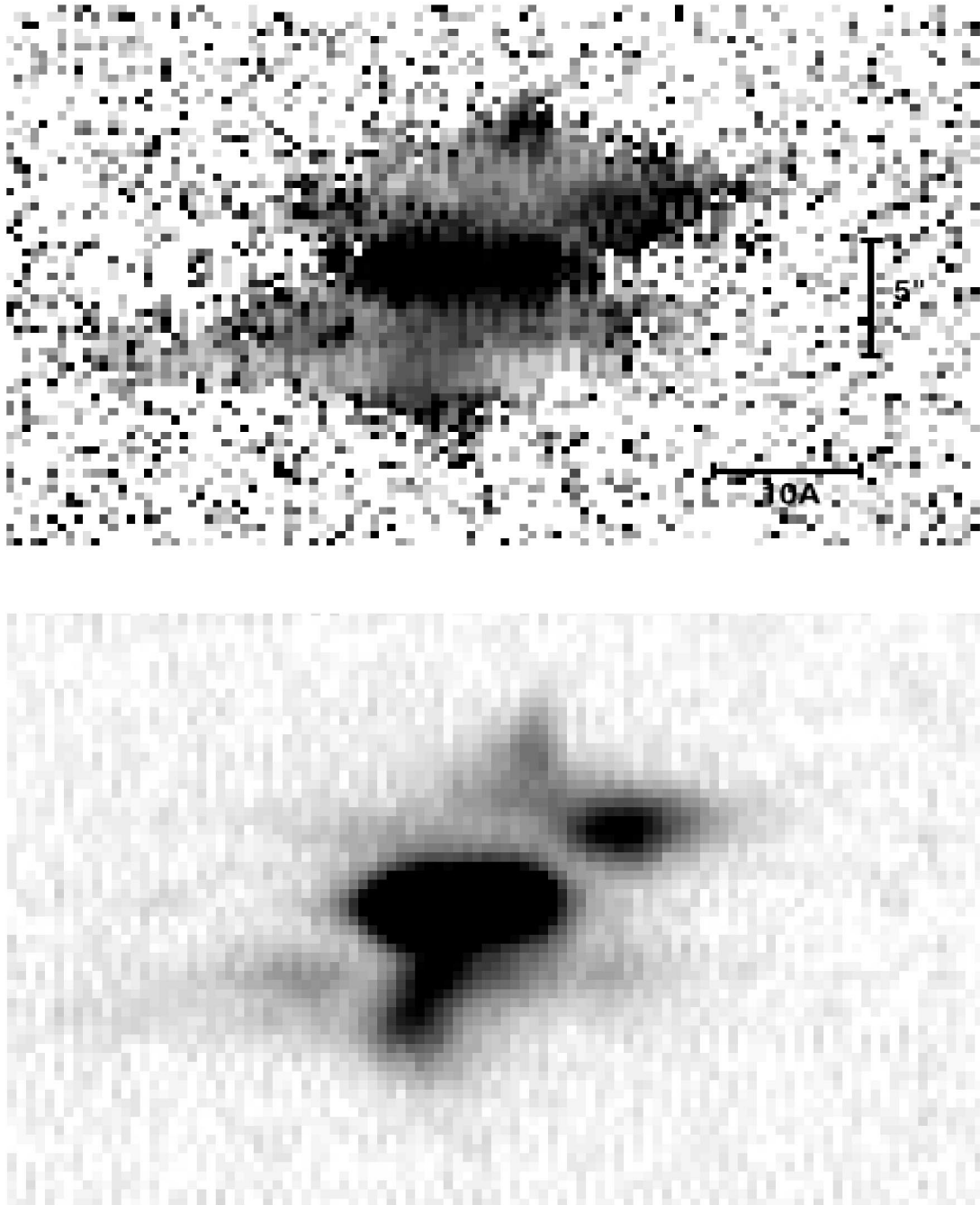


FIG. 15.—Gray-scale representation of (*top*) the variation in the $[\text{O III}](5007)/\text{H}\beta$ ratio—the darkest shades correspond to the largest values for the ratio—with velocity (x -axis) and displacement (y -axis); and for comparison (*bottom*) the continuum-subtracted $[\text{O III}]$ profile. The horizontal and vertical scale bars indicate a wavelength shift of 10 \AA (600 km s^{-1}) and a spatial displacement of $5''$, respectively. The scale is the same for both images, and both were derived from the blue high-dispersion long-slit spectrum. West is to the top; wavelength/redshift increases to the right.

CLARK ET AL. (see 494, 556)

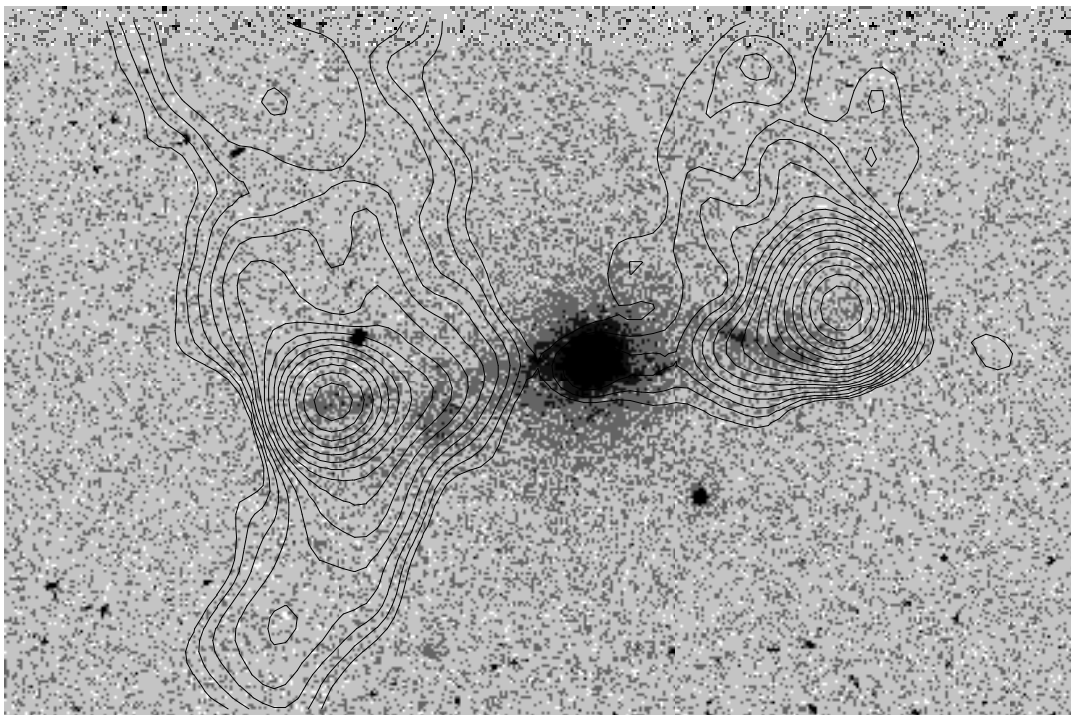
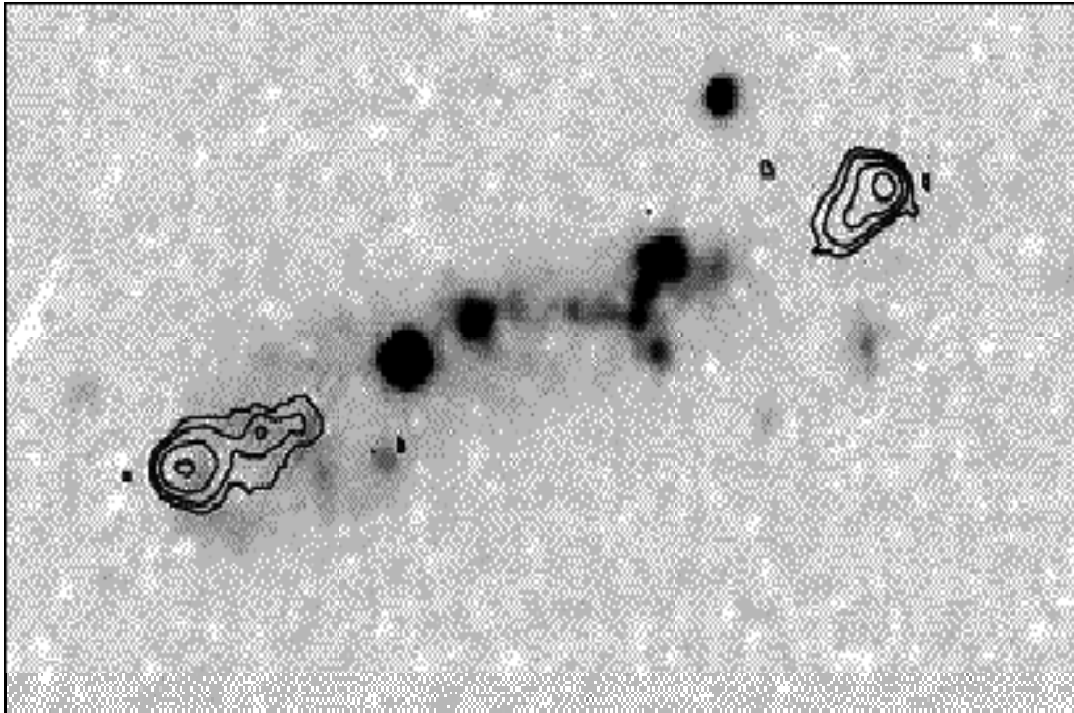


FIG. 22.—Gray-scale representations of the broadband WFPC2 *HST* images of the powerful radio galaxies 3C 368 (*left*) and 3C 171 (*right*), with contours of the VLA radio maps superimposed. Scale and orientation are arbitrary. The 3C 368 image is reproduced courtesy of AURA/STScI.

CLARK ET AL. (see 494, 565)